

Overexpressing Corticotropin-Releasing Hormone in the Primate Amygdala Increases Anxious Temperament and Alters Its Neural Circuit

Ned H. Kalin, Andrew S. Fox, Rothem Kovner, Marissa K. Riedel, Eva M. Fekete, Patrick H. Roseboom, Do P.M. Tromp, Benjamin P. Grabow, Miles E. Olsen, Ethan K. Brodsky, Daniel R. McFarlin, Andrew L. Alexander, Marina E. Emborg, Walter F. Block, Julie L. Fudge, and Jonathan A. Oler

ABSTRACT

BACKGROUND: Nonhuman primate models are critical for understanding mechanisms underlying human psychopathology. We established a nonhuman primate model of anxious temperament (AT) for studying the early-life risk to develop anxiety and depression. Studies have identified the central nucleus of the amygdala (Ce) as an essential component of AT's neural substrates. Corticotropin-releasing hormone (CRH) is expressed in the Ce, has a role in stress, and is linked to psychopathology. Here, in young rhesus monkeys, we combined viral vector technology with assessments of anxiety and multimodal neuroimaging to understand the consequences of chronically increased CRH in the Ce region.

METHODS: Using real-time intraoperative magnetic resonance imaging-guided convection-enhanced delivery, five monkeys received bilateral dorsal amygdala Ce-region infusions of adeno-associated virus serotype 2 containing the CRH construct. Their cagemates served as unoperated control subjects. AT, regional brain metabolism, resting functional magnetic resonance imaging, and diffusion tensor imaging were assessed before and 2 months after viral infusions.

RESULTS: Dorsal amygdala CRH overexpression significantly increased AT and metabolism within the dorsal amygdala. Additionally, we observed changes in metabolism in other AT-related regions, as well as in measures of functional and structural connectivity.

CONCLUSIONS: This study provides a translational roadmap that is important for understanding human psychopathology by combining molecular manipulations used in rodents with behavioral phenotyping and multimodal neuroimaging measures used in humans. The results indicate that chronic CRH overexpression in primates not only increases AT but also affects metabolism and connectivity within components of AT's neural circuitry.

Keywords: AAV2, Central nucleus of the amygdala, DTI, FDG-PET, fMRI, MRI-guided neurosurgery

<http://dx.doi.org/10.1016/j.biopsych.2016.01.010>

Nonhuman primate models are critical for understanding mechanisms underlying the development and expression of human psychopathology (1,2). This is supported by the remarkable correspondence between nonhuman and human primates in brain structure and function that underlies their similarities in behavior, rearing methods, psychosocial development, and cognition (2,3). The imperative to identify new molecular treatment targets to treat psychiatric disorders (4,5), along with the evolutionary linkage between nonhuman and human primates, provides a compelling rationale to develop techniques in nonhuman primates that can alter the function of candidate genes in a targeted brain-region-selective manner. Furthermore, the ability to use multimodal imaging methods to understand the impact of region-specific molecular

manipulations in a relevant primate model allows for understanding the mechanisms associated with altered neural circuits in psychiatric illnesses.

To date, our nonhuman primate studies have focused on establishing a model for investigating mechanisms underlying the development of extreme early-life anxiety (2,6–15). First, we developed and standardized the no eye contact (NEC) condition of the human intruder paradigm to assess individual trait-like differences in anxiety-related behavior in response to potential threat (16). This trait-like disposition, termed anxious temperament (AT), is a prominent childhood risk factor for the later development of anxiety disorders, depression, and comorbid substance abuse (17–21). With our nonhuman primate model, we identified the altered neural circuitry that

underlies the development of AT and found that it is similar to that observed in humans with anxiety disorders (3,8,10,22). This neural system-level information provides the critical groundwork for directly testing regionally specific molecular hypotheses potentially important in the pathophysiology of AT.

When extreme, AT or its major behavioral component, behavioral inhibition, markedly increases a child's risk for the later development of stress-related psychopathology (17–19,23). By combining measures of threat-related behavioral inhibition (increased freezing and decreased vocalizations) and pituitary-adrenal activation (threat-induced cortisol), along with 18 F-fluoro-deoxyglucose positron emission tomography (FDG-PET), in rhesus monkeys, we characterized a non-human primate developmental model of AT (6,14). Although the AT neural circuit is distributed across prefrontal, limbic, and brainstem regions, neuroimaging studies in monkeys and humans point to the dorsal amygdala, a region containing the central nucleus of the amygdala (Ce), as a fundamental component of the circuit (8,10,11) (Figure 1). The Ce is of particular interest because it is the major outflow region of the amygdala with its downstream projections mediating the hypothalamic and brainstem contributions to the stress response (24,25). The Ce is causally involved in mediating AT, as neurotoxic lesions of the rhesus monkey dorsal

amygdala, which encompass the Ce, decrease the expression of behavioral inhibition and pituitary-adrenal activity (26).

The Ce is predominantly composed of gamma-aminobutyric acidergic neurons that also contain numerous modulatory neuropeptides and receptors (27). Within the Ce, there is expression of corticotropin-releasing hormone (CRH) (Figure 1), its two receptors, and its binding protein (28–31). CRH-containing neurons in the paraventricular nucleus of the hypothalamus play a prominent role in mediating the stress-related pituitary-adrenal response. Interestingly, extrahypothalamic brain CRH neurons, including those in the Ce, can be regulated differently (32) and are important in coordinating the autonomic, emotional, behavioral, and cognitive components of the stress response (33,34). Rodent studies have demonstrated that stress increases the expression of CRH in the paraventricular nucleus of the hypothalamus and Ce (35), whereas corticosterone administration decreases expression of CRH in the paraventricular nucleus of the hypothalamus, while concomitantly increasing the expression of Ce CRH (32). In addition to its role in modulating adaptive stress responses, overactivity of the CRH system is hypothesized to be an important pathophysiological mediator of symptoms associated with anxiety and depressive disorders (36). Recent reports suggest that structural variation of genes in the CRH family may contribute to the expression and pathophysiology of human depression and anxiety disorders (37–43), as well as to extreme monkey AT and its associated altered brain metabolism (44).

In addition to the translational value of nonhuman primate models, it is important to emphasize that primates significantly differ from rodents in the distribution and organization of brain CRH systems (31). Rodent studies have used transgenic, viral vector, and other neuronal modulatory strategies to model CRH molecular alterations hypothesized to underlie stress-related psychopathology (45–50). However, these mechanistic studies have not been translated to primate species. Therefore, using a viral vector gene delivery strategy to chronically increase the expression of CRH in the dorsal amygdala of young rhesus monkeys, we aimed to identify the role of amygdala CRH systems in the expression of primate anxiety.

Here, we demonstrate that regional chronic overexpression of a putative anxiogenic neuropeptide results in increased anxiety-like behaviors along with anxiety-related changes in primate brain function. Using a viral vector infused with convection-enhanced delivery and guided by real-time intraoperative magnetic resonance imaging (RT-IMRI), we aimed to chronically overexpress CRH in the Ce region of the amygdala. This approach was combined with multimodal functional and structural brain imaging to test the hypothesis that increased dorsal amygdala CRH would increase AT, as well as glucose metabolism in the Ce. To allow for new insights into how increased amygdala CRH may influence brain-wide neural alterations underlying stress-related psychopathology, we also examined the impact of chronic dorsal amygdala CRH overexpression on functional and structural connectivity with other relevant brain regions. This study provides a framework for further development of preclinical nonhuman primate strategies to evaluate novel, region-specific molecular targets for the treatment of human psychopathology.

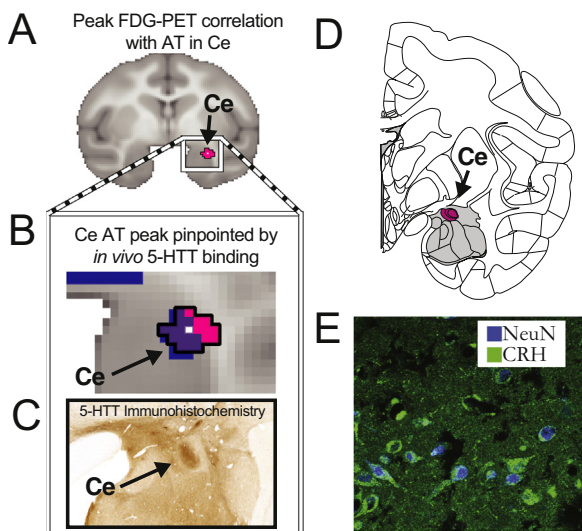


Figure 1. Endogenous corticotropin-releasing hormone (CRH) expression in the anxious temperament (AT)-related central nucleus of the amygdala (Ce) region. **(A)** Using 18 F-fluoro-deoxyglucose positron emission tomography (FDG-PET) imaging, we found that metabolism within the Ce predicted individual differences in AT in young rhesus monkeys. **(B)** The Ce region was defined by its overlap (purple) with serotonin transporter (5-HTT) ligand binding determined with PET imaging (blue). **(C)** The serotonin transporter binding characterized by PET mirrors its neuroanatomical distribution observed with immunohistochemical methods. **(D)** Within this critical primate Ce region, we found **(E)** a moderate amount of endogenous CRH immunoreactivity (green) located in neurons, as defined by the overlap with NeuN expression (blue). [Panel A reprinted with permission from Oler *et al.* (8). Panel C reprinted with permission from O'Rourke and Fudge (98). Panel D adapted with permission from Paxinos *et al.* (99).]

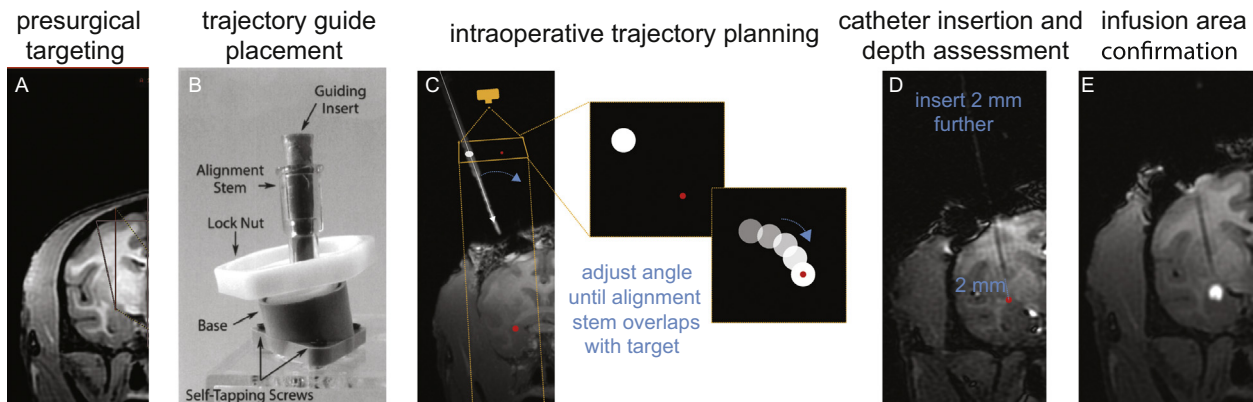


Figure 2. Real-time intraoperative magnetic resonance imaging guided targeting and infusion monitoring. **(A)** Prior to surgery, a structural magnetic resonance image was obtained to visualize the target and plan the trajectory. **(B)** A pivot point-based magnetic resonance imaging compatible external trajectory guide was mounted on the skull. **(C)** Precise targeting was performed by imaging a plane orthogonal to the long axis of the external trajectory guide, as if it were visualized by a camera from above. The inset boxes represent the plane in which the trajectory guide (white dot) is visualized and aligned in relation to the target injection point (red dot). **(D)** The depth of the catheter is advanced to approximately 2 mm above the target. Another magnetic resonance image was acquired to make precise measurements between the catheter tip and the target before advancing the catheter to its final position. **(E)** Immediately after the adeno-associated virus type 2-corticotropin-releasing hormone/gadolinium infusion was complete, a final magnetic resonance image was acquired to verify the infusion delivery region. [Panel B reprinted with permission from Emborg *et al.* (54)].

METHODS AND MATERIALS

Overall Study Design

Behavioral measures of AT and glucose-based measures of brain metabolism (FDG-PET) were assessed during NEC before surgery and again approximately 2 months later in five CRH-overexpressing monkeys and at similar intervals in their five matched unoperated control monkeys. Additionally, magnetic resonance imaging (MRI) measures of structural connectivity with diffusion tensor imaging and functional intrinsic connectivity with resting functional MRI, were acquired before and after surgery. Paired-sample *t* tests controlling for age were used to test for group differences in post-pre measures that resulted from CRH overexpression (i.e., CRH group [post-pre] – control group [post-pre]).

The surgeries were performed using RT-IMRI guidance to localize the target. To estimate the dispersion of adeno-associated virus type 2 (AAV2)-CRH, we infused the viral vector concurrently with the MR visible marker gadobenate dimeglumine (MultiHance, Bracco Diagnostics, Monroe Township, NJ). To characterize the pattern of CRH expression, animals were euthanized approximately 1 year after surgery and immunohistochemical staining for CRH was performed approximately 10 months after the behavioral assessments.

Note that space limitations do not allow for a complete description of the methods in the body of the article and much of the methodological detail concerning the surgery and brain imaging analyses (FDG-PET, functional MRI, and diffusion tensor imaging) can be found in the [Supplement](#).

Subjects

First, two cynomolgus monkeys (*Macaca fascicularis*) were used in pilot studies to 1) demonstrate the effectiveness of the AAV2-CRH virus to direct CRH overexpression *in vivo*, and 2) to visualize endogenous CRH expression in the Ce ([Supplement](#)). Next, 10 young male rhesus monkeys (*Macaca*

mulatta) (1.76–2.63 years old, 2.77–5.25 kg) were used in the CRH overexpression experiment. These animals were screened with the human intruder paradigm and were selected to be in the midrange for freezing responses. Five animals received bilateral infusions (two infusions per hemisphere) of AAV2-CRH into the dorsal amygdala Ce region. The other five nonoperated control animals were age-matched and pair-housed with each of their corresponding transfected monkeys. Because of considerations related to performing unnecessary procedures on nonhuman primates and because we have used nonoperated control animals to successfully examine lesion-induced effects on primate anxiety in previous studies (26,51,52), we chose to use nonoperated cagemates as control subjects. Animals were housed and cared for at the Harlow Center for Biological Psychology and the Wisconsin National Primate Research Center on a 12-hour light/dark cycle, in a temperature- and humidity-controlled vivarium. For all imaging and surgical procedures, the animals were fasted overnight. The experiments were performed according to the federal guidelines of animal use and care (53) and with approval of University of Wisconsin-Madison Institutional Animal Care and Use Committees.

Characterizing Anxious Temperament and Glucose Metabolism During NEC

AT was characterized using the NEC condition of the human intruder paradigm and was computed as the combination of standardized freezing, cooing, and cortisol measures (6,14). NEC assessment coincided with the administration of FDG followed by small-animal positron emission tomography scanning (see the [Supplement](#) for further details).

Real-Time Intraoperative MRI

Placement of the MRI-compatible trajectory guide bases followed previously reported methods [see (54,55) for details]

modified for Ce targeting (Figure 2). The intraoperative targeting was performed using a platform for real-time MR-guided prospective stereotaxy (56) that was initially developed by the University of Wisconsin (57–60). A detailed description of the RT-IMRI methods can be found in the Supplement. The rhesus Ce is approximately 5 mm long in the anterior-posterior plane and approximately 1 to 2 mm in the dorsal-ventral and medial-lateral planes. To cover as much of the Ce as possible while minimizing treatment to surrounding regions, two 12- μ L infusions were performed per hemisphere (one anterior Ce target, one posterior Ce target), for a total of 24 μ L per hemisphere. After each infusion, the catheter was removed, and after all infusions were complete, the animal was transported back to the surgical suite and the craniotomies were closed.

Assessing CRH Overexpression

Approximately 1 year after AAV2 infusions, the animals were euthanized. The brains were extracted and fixed overnight in 4% paraformaldehyde, cryoprotected, and then sectioned at 40 μ m. CRH immunoreactivity was assessed as described in the Supplement. Every twelfth section through the brain was immunostained for CRH. Adjacent coronal brain sections were processed for acetylcholinesterase, a cholinergic marker that facilitates anatomical identification of amygdala nuclei and subnuclei (61).

For each animal, the distribution of CRH-positive cells was charted through the rostrocaudal extent of the Ce region using camera lucida techniques. Sections were initially drawn under bright-field illumination at 1.6 \times , to include labeled cells and landmarks such as blood vessels and fiber tracks. The distribution of labeled cells was then confirmed under 10 \times bright-field illumination. Adjacent acetylcholinesterase-stained sections were then viewed under dark-field illumination, using landmarks in the charted sections for alignment. This permitted overlay of acetylcholinesterase-determined boundaries of amygdala nuclei and subnuclei for each section. Finally, paper maps were digitized using a drawing tablet in conjunction with the program Adobe Illustrator CS2 (Adobe Systems, San Jose, CA).

To compare the relative distribution of labeled cells resulting from viral-mediated CRH expression and/or endogenous CRH expression across animals, we overlaid individual maps from each animal upon one another in transparent layers, matching rostrocaudal levels as closely as possible. Labeled cells for each pair of animals were color-coded to assist in the analysis.

RESULTS

Characterization of CRH Overexpression

Postmortem immunocytochemical analyses demonstrated marked overexpression of CRH in the dorsal amygdala region of the experimental animals compared with the levels of endogenous CRH in the control animals. The RT-IMRI gadobenate dimeglumine infusion scan from each animal was compared with the animal's pattern of CRH overexpression defined by immunocytochemistry (Figure 3). As can be seen in Figure 4A, in all experimental animals, CRH overexpression was evident in the dorsal amygdala including

regions of the lateral and medial divisions of the Ce as well as in surrounding areas such as the dorsal regions of the accessory basal nucleus, the magnocellular region of the basal nucleus, the amygdala striatal transition zone, and portions of the ventral putamen (Table 1). We found that across all transfected animals the extent and location of the infusions as determined by RT-IMRI matched the areas of CRH overexpression determined with immunocytochemistry (compare Figure 4A and Figure 3E). This demonstrates the ability to use in vivo imaging methods to estimate the extent of infusion as well as AAV2-CRH transfection after 1 year.

Effects of CRH Overexpression on AT and Brain Metabolism

As predicted, compared with control animals, the CRH overexpressing animals demonstrated a significant increase in AT (CRH group_[post-pre] – control group_[post-pre]) ($p < .05$, one-tailed; Figure 5). A complementary unpaired between-groups analysis (controlling for age as in the paired analysis) revealed significant group differences in the AT phenotype ($t = 2.040$, $p = .0405$, one-tailed; see Supplemental Figure S3). It is noteworthy that CRH concentrations in cerebrospinal fluid (CSF) did not significantly differ between experimental and control animals (see Supplemental Methods and Results). Corresponding analyses of FDG-PET data revealed that CRH overexpression also resulted in significant increases in dorsal amygdala metabolism ($p < .01$, uncorrected; Figure 6A). Additional whole-brain voxelwise analyses revealed that the CRH overexpression animals had significantly greater increases in metabolism in orbital preoccipital/anterior insular cortices (OPro/AI) and hippocampus ($p < .01$, two-tailed, uncorrected; Figure 6A and Supplemental Table S1). It is important to underscore that these regions have been implicated as part of the AT network, as well as in human anxiety disorders. To identify regions across both control and experimental animals in which post-pre changes in AT were predicted by changes in metabolism, we looked within brain regions that demonstrated an effect of CRH overexpression (Figure 6B, yellow outline). This analysis revealed that regardless of treatment condition, changes in AT from the presurgical to postsurgical assessment were predicted by individual differences in metabolic increases in regions of the dorsal amygdala, OPro/AI, and hippocampus (red, $p < .05$, two-tailed, uncorrected; Figure 6B and Supplemental Table S2). These findings suggest that the effects of dorsal amygdala CRH overexpression on increasing AT involve activation of this distributed neural circuit.

Effects of CRH Overexpression on Functional Connectivity and White Matter Integrity

The functional MRI data demonstrated that chronic CRH overexpression altered resting functional connectivity. The dorsal amygdala seed region for the functional connectivity analyses was determined by the overlap of the infusion area detected with gadobenate dimeglumine (see yellow region in Figure 3E) with that of the metabolic region that was affected by CRH overexpression (see yellow region in Figure 6A, right). Results demonstrated that CRH overexpression altered functional connectivity such that connectivity with the right dorsal

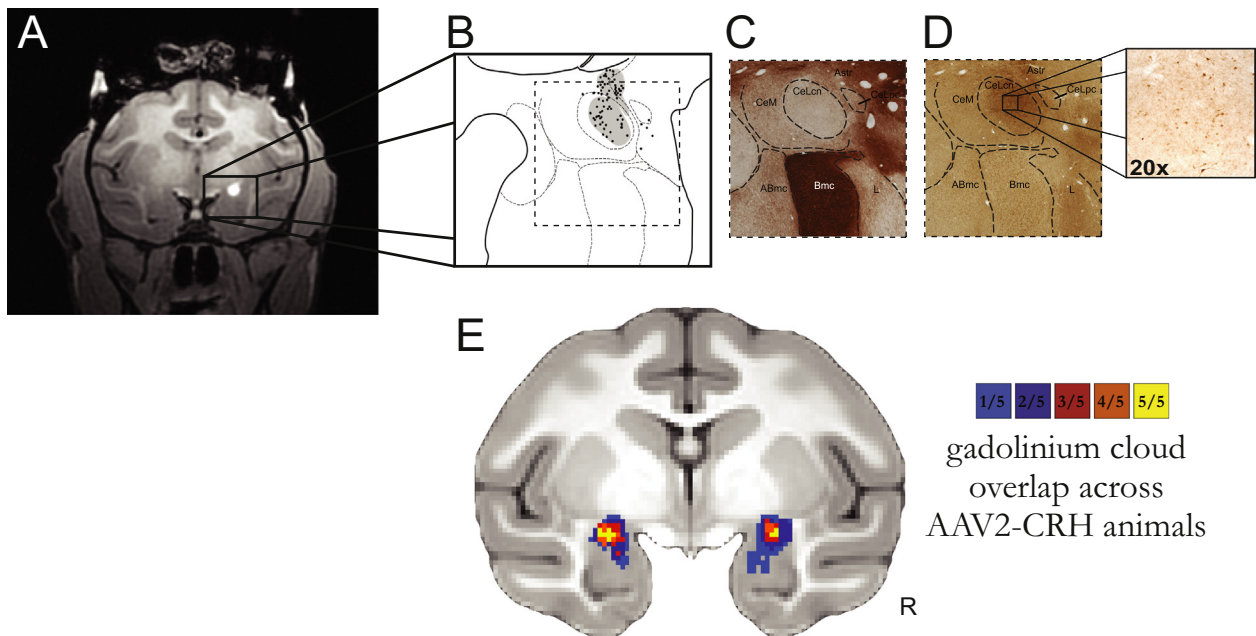


Figure 3. In vivo estimation and postmortem verification of dorsal amygdala corticotropin-releasing hormone (CRH) overexpression. **(A)** The gadolinium clouds in the dorsal amygdala, central nucleus of the amygdala (Ce) region, during and immediately following adeno-associated virus type 2 (AAV2)-CRH delivery provided an estimate of the location and extent of the infusions. **(B)** Camera lucida drawings of CRH expression from postmortem tissue reflected the extent of viral infusion as estimated from the intraoperative gadolinium signal. Gray regions in **(B)** represent neuropil staining and the black dots represent CRH overexpressing cells. **(C)** Acetylcholinesterase staining defined the boundaries of the amygdalar nuclei. Note the relative absence of acetylcholinesterase staining in the central nucleus, lateral central subdivision (CeLcn). **(D)** Adjacent sections were used for CRH immunohistochemistry demonstrating marked overexpression in the dorsal amygdala, Ce region. **(E)** Quantification of gadolinium diffusion extent and cross-subject overlap. Based on the intraoperative gadolinium images, we estimated the infusion extent in standard magnetic resonance imaging space. This allows for an estimation of the across-subject overlap of CRH expression and provides a link to the postmortem CRH expression data (compare with Figure 4A). The overlap of the gadolinium injection clouds across all five experimental animals demonstrates the replicability of the magnetic resonance imaging-guided targeting procedure. The colors represent the number of animals with gadolinium signal at each voxel. Note the bilateral overlap across all experimental animals within the Ce region (yellow). ABmc, accessory basal nucleus, magnocellular subdivision; Astr, amygdalostriatal transition zone; Bmc, basal nucleus, magnocellular subdivision; CeLpc, central nucleus, lateral central subdivision; CeM, central nucleus, medial subdivision; L, lateral nucleus; R, right.

amygdala seed in various regions differed between groups ($p < .01$, two-tailed, uncorrected; Supplemental Table S3). Of note, increased connectivity was found between right dorsal amygdala and regions encompassing bilateral portions of OPro/AI.

Analyses of the diffusion tensor imaging data were performed to examine effects of long-term CRH overexpression on white matter microstructure. Voxelwise analyses were performed on measures of diffusivity and fractional anisotropy (FA). Investigation of mean diffusivity, axial diffusivity, and radial diffusivity demonstrated significant alterations in various regions (Supplemental Tables S4–S6). Of particular interest, CRH overexpression in the dorsal amygdala was associated with significant increases in mean diffusivity, axial diffusivity, and radial diffusivity in a region of the brain that overlaps with the extended amygdala/bed nucleus of the stria terminalis ($p < .005$, two-tailed, uncorrected). Such an increase in mean diffusivity, axial diffusivity, and radial diffusivity can be indicative of decreased density of microstructure but can also be explained by increased levels of CSF. Since this region is proximal to the ventricles, this possibility should be considered.

Analysis of FA, an overall indicator of white matter integrity, demonstrated that dorsal amygdala-CRH overexpression

resulted in decreased FA in various regions including portions of the medial/midline thalamus ($p < .005$, two-tailed, uncorrected; Figure 7 and Supplemental Table S7). This region of medial thalamus encompasses the ventral edge of the medial dorsal thalamus, portions of the central medial and paracentral thalamic nuclei, as well as the magnocellular division of the ventral anterior thalamic nucleus. Fiber tractography enabled an investigation of the connectivity of this region with the rest of the brain (Supplement and Supplemental Figure S4).

DISCUSSION

In this study, we validated methods combining RT-IMRI with convection-enhanced delivery to reliably locate and accurately infuse AAV2-CRH into the primate Ce region. This demonstrates the feasibility of translating rodent mechanistic studies that directly manipulate gene function in the brain to primates and implicates overactive brain CRH systems in the pathophysiology of excessive primate anxiety. These findings further point to the dorsal amygdala, Ce region, as a key site involved in determining individual differences in dispositional anxiety and the phenotype that represents the risk to develop stress-related psychopathology. This study is the first to use viral vector strategies in nonhuman primates to directly manipulate



Figure 4. Quantification of dorsal amygdala corticotropin-releasing hormone (CRH) expression. **(A)** Postmortem analyses demonstrated overexpression of CRH in the dorsal amygdala and surrounding regions in the experimental animals, compared with **(B)** the levels of endogenous CRH observed in the cagemate control animals (top = anterior, bottom = posterior). Each pair of animals is represented by a different color in the composite image, and each dot represents a CRH-expressing cell body. Note that endogenous CRH expression levels in control animals were found in the most posterior regions of the central nucleus of the amygdala (only the left hemisphere is presented) and were substantially lower than that induced by adeno-associated virus type 2 (AAV2)-CRH transfection. AAA, anterior amygdaloid area; ABmc, accessory basal nucleus, magnocellular subdivision; AC, anterior commissure; Astr, amygdalostratial transition zone; BMC, basal nucleus, magnocellular subdivision; CeLcn, central nucleus, lateral central subdivision; CeLpc, central nucleus, lateral paracapsular subdivision; CeM, central nucleus, medial subdivision; H, hippocampus; L, lateral nucleus; M, medial nucleus; nbm, nucleus basalis of Meynert; P, putamen; V, ventricle.

CRH molecular systems hypothesized to be involved in human psychiatric disorders. Our primate model provides a unique opportunity to assess the effects of gene manipulation on primate behavior in conjunction with the same in vivo measures of brain function and structure that are used to assess human neuropsychiatric patients.

While much of the mechanistic work focused on the role of CRH in anxiety and fear has been performed in rodents, a few studies have been done in primates. Because of the similarities in brain function and structure, behavior, and social functioning between nonhuman primates and humans, rhesus monkeys provide an important and valuable model for

Table 1. Relative Density of CRH-Labeled Cells in Both Hemispheres, Summing Across All Rostrocaudal Levels

Case	CeLcn/pc	CeM	Bmc	ABmc	Astr	Ventral Putamen
CRH-1	++	++	++	+++++	+++++	+++
CRH-2	++	+	+++++	+++++	+++++	+++++
CRH-3	+++	+	+++++	+	+++++	+++++
CRH-4	+++	++	+	+++++	+++++	+
CRH-5	+++	+++	+++++	+++++	+++++	+++++
CON-1	+					
CON-2	+					
CON-3	+					
CON-4	+					
CON-5	+					

ABmc, accessory basal nucleus, magnocellular subdivision; Astr, amygdalostratial transition zone; Bmc, basal nucleus, magnocellular subdivision; CeLcn/pc, central nucleus, lateral central subdivision/paracapsular subdivision; CeM, central nucleus, medial subdivision; CON, control; CRH, corticotropin-releasing hormone.

studying human psychopathology. The marked difference in distribution of brain CRH receptors between rodents and primates further supports the use of primates for studies of stress-related psychopathology. For example, primates have both CRH receptor 1 (CRHR1) and CRH receptor 2 (CRHR2) in the Ce, whereas the rodent Ce is only populated with CRHR1 (31,62). Early rodent studies site-specifically administering CRH or CRH antagonists established a key role for the amygdala, including the Ce, as being important in mediating the effects of CRH on anxiety and fear responses (63–69). Other studies suggest that within the rodent Ce, it is likely that CRH acts via activation of CRHR1 (70–72). Additionally, mouse transgenic and knockout studies manipulating expression of CRH or CRHR1 demonstrated an important role for CRH systems in mediating adaptive and maladaptive behavioral and physiological responses to stress [for review, see (73)]. Because of the presence of CRHR2 receptors in the

primate Ce, it is possible that the anxiogenic effects of CRH are mediated by activation of CRHR2 receptors.

Our early work in rhesus monkeys is consistent with results from the rodent studies. For example, we demonstrated that intraventricularly administered CRH increased anxiety when administered at low doses and at higher doses resulted in depressive-like behaviors (74). Because of the wide distribution of CRH receptors throughout the brain (31,62,75,76), it is likely that these effects were mediated by activation of CRH receptors in diverse brain regions—a finding that is supported by brain-wide metabolic brain changes seen following very high doses of intraventricular CRH (77). In another study, we also reported a relation between CSF levels of CRH and threat-induced behavioral inhibition (78); however, this finding has not been replicated (Ned Kalin, M.D., unpublished data, 2015). It is important to note that some, but not all, human studies demonstrate increased CSF CRH concentrations associated with depression and/or suicide (79) and postmortem analyses of suicide victims have revealed increased activity in brain CRH systems (80–84). Neurotoxic lesion studies in primates demonstrated that Ce lesions not only reduced anxiety but also decreased concentrations of CSF CRH (26). Thus, in the Ce lesion study, the reduction in anxiety could be accounted for by the global reduction in CSF CRH. In the current study, in which we used a viral vector strategy to overexpress CRH in the dorsal amygdala region, anxiety and brain function were affected in the absence of a detectable increase in CSF CRH levels. Taken together, these findings suggest that while CRH can have profound impacts throughout the brain, the Ce is a site that is critically involved in mediating these effects.

Recent viral vector studies in rodents have implicated the chronic overexpression of Ce CRH in inducing anxiety- and depression-related behaviors (46,48,49,85,86). In general, but not always, overexpression of Ce CRH is reported to affect physiological parameters such as the startle response and hypothalamic-pituitary-adrenal activity (48,49,85,86). Our current findings in nonhuman primates are consistent as we demonstrate that overexpression of CRH increases AT.

With the functional and structural brain imaging measures used in our study, we were able to extend the rodent studies by examining the impact of chronically increased dorsal amygdala CRH on brain metabolism, as well as functional and structural connectivity. These analyses provide potential insights into mechanisms underlying the neural circuit alterations associated with human anxiety and other stress-related psychopathologies. Our data are the first to demonstrate that an overactive amygdala CRH system has local effects on brain metabolic activity as well as on other components of the neural circuit associated with anxiety and AT. Specifically, we found that CRH overexpression resulted in increased metabolism in posterior regions of the orbitofrontal cortex (OPro), anterior insula, and hippocampus. Since the areas of overexpression encompassed Ce, other dorsal regions of the amygdala, and neighboring structures (e.g., putamen), it is possible that CRH expression in these different regions contributed to the observed effects. Additionally, we found evidence that in some cases the virus was anterogradely and/or retrogradely transported to other brain regions that are monosynaptically connected to the site of infusion.

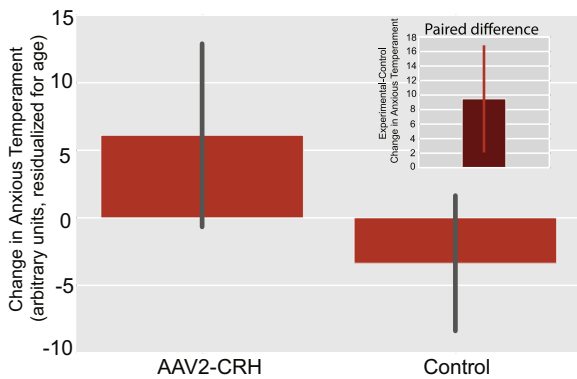


Figure 5. Corticotropin-releasing hormone (CRH) overexpressing animals demonstrated a significant increase in anxious temperament. Compared with their matched control animals, the CRH overexpressing animals demonstrated increased postsurgical levels of anxious temperament (mean \pm SEM). Significance was determined using a paired-samples *t* test comparing dorsal amygdala CRH animals and their cagemate control animals (CRH group_[post-pre] – control group_[post-pre]) ($p < .05$, one-tailed; see inset and Methods and Materials for details). AAV2, adeno-associated virus type 2.

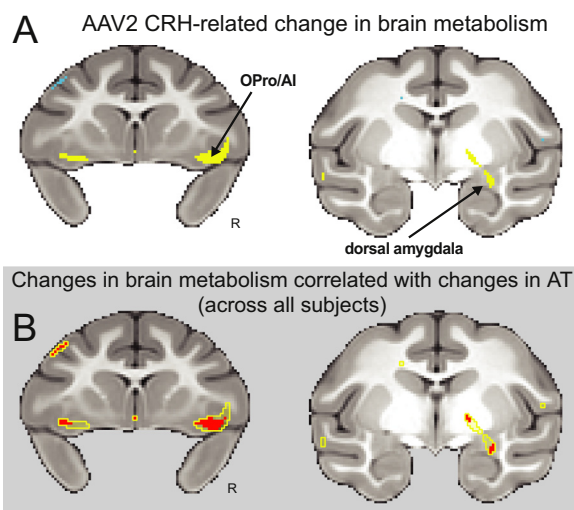


Figure 6. Corticotropin-releasing hormone (CRH) overexpressing animals demonstrated significant increases in brain metabolism. **(A)** Compared with their matched control animals, the CRH overexpressing animals demonstrated increased post-pre change in metabolism within the dorsal amygdala, orbital preoccipital/anterior insular cortices (OPro/AI), and hippocampus (yellow, $p < .01$, two-tailed, uncorrected; Supplemental Table S1). All of these regions have been implicated in anxious temperament (AT). **(B)** Within regions that were affected by CRH overexpression (yellow outline), we identified areas in which the post-pre change in metabolism correlated with the post-pre change in AT (red; $p < .05$, one-tailed, uncorrected). Across all 10 animals, changes in AT were associated with changes in brain metabolism in the dorsal amygdala and in bilateral regions of the posterior OPro/AI. AAV2, adeno-associated virus type 2; R, right.

We also found that dorsal amygdala CRH overexpression increased functional connectivity between this area and the OPro/AI region of posterior orbital cortex. The findings regarding the OPro/AI region may be particularly relevant, as this region of the prefrontal cortex is highly connected with the amygdala (87). We recently demonstrated in a sample of 592 young rhesus monkeys that NEC-related glucose metabolism in the OPro/AI region (along with the bed nucleus of the stria terminalis and the periaqueductal gray) correlated with AT and was heritable (10). Importantly, brain metabolism in these regions was also genetically correlated with AT, which implies the involvement of similar genes in mediating AT and altered brain function in OPro/AI, bed nucleus of the stria terminalis, and periaqueductal gray.

Perhaps even more interesting are the structural brain changes that were associated with long-term increased CRH overexpression. Using measures of white matter integrity, we found evidence for decreases in FA in the medial thalamus encompassing portions of the central medial thalamic nucleus, paracentral thalamic nucleus, and the magnocellular division of the ventral anterior thalamic nucleus. Primate studies demonstrate that these regions contain CRH-immunoreactive cell bodies and fibers, as well as relatively high densities of CRHR1 (31,88,89). It is therefore possible that overexpression of CRH in the dorsal amygdala could lead to increased activation of medial thalamic CRHR1. Tractography methods demonstrated that white matter fibers link the thalamic region of significant FA change with other components of the neural network important in the expression and regulation of anxiety

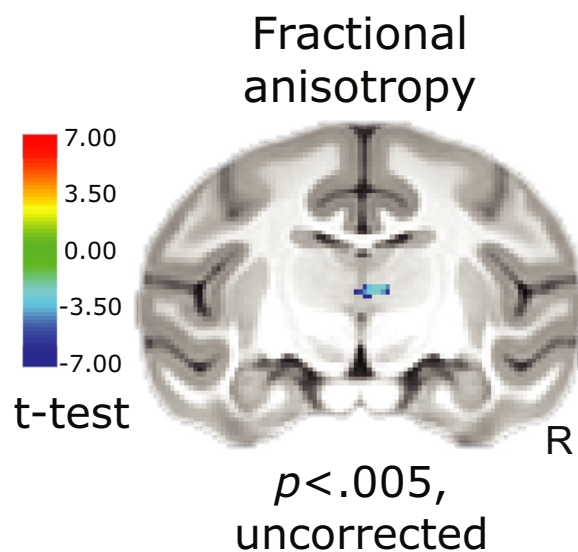


Figure 7. Diffusion tensor imaging demonstrated altered thalamic structural integrity as assessed with fractional anisotropy. Whole-brain voxelwise analyses indicated corticotropin-releasing hormone-induced reductions in fractional anisotropy in a region overlapping with the medial dorsal/midline thalamus (corticotropin-releasing hormone group _[post-pre] – control group _[post-pre]) ($p < .005$, uncorrected). Deterministic tractography demonstrates that this thalamic region is connected to the prefrontal cortex and medial temporal lobe (Supplemental Figure S4). R, right.

(Supplemental Figure S4). This is consistent with ex vivo tract tracing studies in macaques that demonstrate projections from the dorsal amygdala to midline thalamic nuclei (90,91). Also, medial thalamic nuclei are reciprocally connected to posterior orbitofrontal cortex regions that include the OPro/AI (92). Thus, the medial/midline thalamus may link dorsal amygdala CRH to metabolic changes in the OPro/AI.

Early excitement related to developing new treatments for human anxiety and depression resulted from numerous mechanistic studies, mostly performed in rodents, directly manipulating brain CRH systems [for reviews, see (93,94)]. Although findings from these studies failed to be translated to positive outcomes in human CRHR1 antagonist clinical trials (95–97), our current findings suggest that continued pursuit of mechanisms directed at altering Ce CRH function in primates might be useful for providing insights into optimizing CRH-altering treatments for human disorders. For example, it may be worth performing human studies targeting CRHR2 because of the possibility that CRHR2 could mediate the effects we observed. Our study also underscores the potential for gene delivery in primate models to elucidate the mechanisms of regional gene expression on distributed brain function, as well as to explore novel treatment strategies for refractory psychiatric illnesses. Taken together, these results indicate that chronically increased dorsal amygdala CRH expression influences AT, metabolic activity within AT's neural substrates, as well as long-range functional connectivity and white-matter microstructure. This work, aimed at understanding the effects of increased CRH in the dorsal amygdala, will help motivate the design of novel interventions to prevent the development of anxiety disorders and other stress-related psychopathology.

ACKNOWLEDGMENTS AND DISCLOSURES

This work was supported by the National Institutes of Health Grant Nos. R01-MH046729 (to NHK), R01-MH63291 (to JLF), R24-OD019803 (to MEE), R43-CA177205 (to WFB, ALA, and EKB), T32-EB011434 (to MEO), T32-MH018931 (to RK), P51-OD011106 (Wisconsin National Primate Research Center, University of Wisconsin-Madison) and by the WARF Accelerator Program.

We thank the personnel of the Harlow Center for Biological Psychology, the HealthEmotions Research Institute, the Waisman Laboratory for Brain Imaging and Behavior, the Wisconsin National Primate Research Center, and the Wisconsin Institutes for Medical Research; K. Brunner; A. Shackman; M. Jesson; L. Williams; D. Hsu; S. Shelton; H. Van Valkenberg; and N. Alcock.

Preliminary versions of this work were presented in poster form at the Society for Neuroscience meeting in Washington, DC, November 15–19, 2014; the American College of Neuropsychopharmacology meeting in Phoenix, Arizona, December 7–11, 2014; and the Society of Biological Psychiatry meeting in Toronto, Ontario, May 14–16, 2015.

Drs. Alexander, Block, and Brodsky are part owners of TherVoyant, Inc., which provided technology that was used for navigation and monitoring of the infusion experiments. Dr. Kalin has received honoraria from CME Outfitters, Elsevier, and the Pritzker Neuropsychiatric Disorders Research Consortium. He is on the Advisory Boards for Corcept Therapeutics and Skyland Trail—George West Mental Health Foundation. Dr. Kalin is a Stockholder in Corcept Therapeutics, and, along with Dr. Roseboom, owns the following patents: promoter sequences for corticotropin-releasing factor alpha (U.S. Patent #7071323, issued on 07-04-06); a method of identifying agents that alter the activity of the promoter sequences (U.S. Patent #7531356, issued on 05-12-09); promoter sequences for urocortin II and the use thereof (U.S. Patent #7087385, issued on 08-08-06); and promoter sequences for corticotropin-releasing factor binding protein and use thereof (U.S. Patent #7122650, issued on 10-17-06). All other authors report no biomedical financial interests or potential conflicts of interest.

ARTICLE INFORMATION

From the Department of Psychiatry (NHK, ASF, RK, MKR, EMF, PHR, DPMT, DRM, ALA, JAO), Neuroscience Training Program (NHK, RK, PHR, DPMT, MEE), Department of Medical Physics (BPG, MEO, EKB, ALA, MEE, WFB), Department of Biomedical Engineering (WFB), Department of Radiology (WFB, EKB) University of Wisconsin; Wisconsin National Primate Research Center (NHK, MEE); and TherVoyant, Inc. (EKB, ALA, WFB), Madison, Wisconsin; and Departments of Neuroscience and Psychiatry (JLF), University of Rochester Medical Center, Rochester, New York.

Address correspondence to Jonathan A Oler, Ph.D., University of Wisconsin School of Medicine and Public Health, Department of Psychiatry, 6001 Research Park Boulevard, Madison, WI 53719; E-mail: oler@wisc.edu.

Received Aug 12, 2015; revised Dec 23, 2015; accepted Jan 14, 2016.

Supplementary material cited in this article is available online at <http://dx.doi.org/10.1016/j.biopsych.2016.01.010>.

REFERENCES

- Nelson EE, Winslow JT (2009): Non-human primates: Model animals for developmental psychopathology. *Neuropsychopharmacology* 34: 90–105.
- Kalin NH, Shelton SE (2003): Nonhuman primate models to study anxiety, emotion regulation, and psychopathology. *Ann N Y Acad Sci* 1008:189–200.
- Fox AS, Kalin NH (2014): A translational neuroscience approach to understanding the development of social anxiety disorder and its pathophysiology. *Am J Psychiatry* 171:1162–1173.
- Insel TR (2012): Next-generation treatments for mental disorders. *Sci Transl Med* 4: 155ps19.
- Hyman SE (2014): The unconscionable gap between what we know and what we do. *Sci Transl Med* 6: 253cm9.
- Fox AS, Shelton SE, Oakes TR, Davidson RJ, Kalin NH (2008): Trait-like brain activity during adolescence predicts anxious temperament in primates. *PLoS One* 3:e2570.
- Kalin NH, Shelton SE, Fox AS, Oakes TR, Davidson RJ (2005): Brain regions associated with the expression and contextual regulation of anxiety in primates. *Biol Psychiatry* 58:796–804.
- Oler JA, Fox AS, Shelton SE, Rogers J, Dyer TD, Davidson RJ, et al. (2010): Amygdalar and hippocampal substrates of anxious temperament differ in their heritability. *Nature* 466:864–868.
- Alisch RS, Chopra P, Fox AS, Chen K, White AT, Roseboom PH, et al. (2014): Differentially methylated plasticity genes in the amygdala of young primates are linked to anxious temperament, an at risk phenotype for anxiety and depressive disorders. *J Neurosci* 34: 15548–15556.
- Fox AS, Oler JA, Shackman AJ, Shelton SE, Raveendran M, McKay DR, et al. (2015): Intergenerational neural mediators of early-life anxious temperament. *Proc Natl Acad Sci U S A* 112:9118–9122.
- Fox AS, Oler JA, Shelton SE, Nanda SA, Davidson RJ, Roseboom PH, Kalin NH (2012): Central amygdala nucleus (Ce) gene expression linked to increased trait-like Ce metabolism and anxious temperament in young primates. *Proc Natl Acad Sci U S A* 109:18108–18113.
- Oler JA, Fox AS, Shelton SE, Christian BT, Murali D, Oakes TR, et al. (2009): Serotonin transporter availability in the amygdala and bed nucleus of the stria terminalis predicts anxious temperament and brain glucose metabolic activity. *J Neurosci* 29:9961–9966.
- Roseboom PH, Nanda SA, Fox AS, Oler JA, Shackman AJ, Shelton SE, et al. (2014): Neuropeptide Y receptor gene expression in the primate amygdala predicts anxious temperament and brain metabolism. *Biol Psychiatry* 76:850–857.
- Shackman AJ, Fox AS, Oler JA, Shelton SE, Davidson RJ, Kalin NH (2013): Neural mechanisms underlying heterogeneity in the presentation of anxious temperament. *Proc Natl Acad Sci U S A* 110: 6145–6150.
- Fox AS, Oakes TR, Shelton SE, Converse AK, Davidson RJ, Kalin NH (2005): Calling for help is independently modulated by brain systems underlying goal-directed behavior and threat perception. *Proc Natl Acad Sci U S A* 102:4176–4179.
- Kalin NH, Shelton SE (1989): Defensive behaviors in infant rhesus monkeys: Environmental cues and neurochemical regulation. *Science* 243:1718–1721.
- Fox NA, Henderson HA, Marshall PJ, Nichols KE, Ghera MM (2005): Behavioral inhibition: Linking biology and behavior within a developmental framework. *Annu Rev Psychol* 56:235–262.
- Clauss JA, Blackford JU (2012): Behavioral inhibition and risk for developing social anxiety disorder: A meta-analytic study. *J Am Acad Child Adolesc Psychiatry* 51:1066–1075.
- Gladstone GL, Parker GB (2006): Is behavioral inhibition a risk factor for depression? *J Affect Disord* 95:85–94.
- Beesdo K, Bittner A, Pine DS, Stein MB, Hofler M, Lieb R, Wittchen HU (2007): Incidence of social anxiety disorder and the consistent risk for secondary depression in the first three decades of life. *Arch Gen Psychiatry* 64:903–912.
- Caspi A, Moffitt TE, Newman DL, Silva PA (1996): Behavioral observations at age 3 years predict adult psychiatric disorders. Longitudinal evidence from a birth cohort. *Arch Gen Psychiatry* 53: 1033–1039.
- Birn RM, Shackman AJ, Oler JA, Williams LE, McFarlin DR, Rogers GM, et al. (2014): Evolutionarily conserved prefrontal-amygdalar dysfunction in early-life anxiety. *Mol Psychiatry* 19:915–922.
- Essex MJ, Klein MH, Slattery MJ, Goldsmith HH, Kalin NH (2010): Early risk factors and developmental pathways to chronic high inhibition and social anxiety disorder in adolescence. *Am J Psychiatry* 167:40–46.
- Davis M, Whalen PJ (2001): The amygdala: Vigilance and emotion. *Mol Psychiatry* 6:13–34.
- Janak PH, Tye KM (2015): From circuits to behaviour in the amygdala. *Nature* 517:284–292.
- Kalin NH, Shelton SE, Davidson RJ (2004): The role of the central nucleus of the amygdala in mediating fear and anxiety in the primate. *J Neurosci* 24:5506–5515.
- Swanson LW, Petrovich GD (1998): What is the amygdala? *Trends Neurosci* 21:323–331.

28. Potter E, Behan DP, Linton EA, Lowry PJ, Sawchenko PE, Vale WW (1992): The central distribution of corticotropin-releasing factor (CRF)-binding protein predicts multiple sites and modes of interaction with CRF. *Proc Natl Acad Sci U S A* 89: 4192–4196.
29. Potter E, Sutton S, Donaldson C, Chen R, Perrin M, Lewis K, *et al.* (1994): Distribution of corticotropin-releasing factor receptor mRNA expression in the rat brain and pituitary. *Proc Natl Acad Sci U S A* 91: 8777–8781.
30. Swanson LW, Sawchenko PE, Rivier J, Vale WW (1983): Organization of ovine corticotropin-releasing factor immunoreactive cells and fibers in the rat brain: An immunohistochemical study. *Neuroendocrinology* 36:165–186.
31. Sanchez MM, Young LJ, Plotsky PM, Insel TR (1999): Autoradiographic and in situ hybridization localization of corticotropin-releasing factor 1 and 2 receptors in nonhuman primate brain. *J Comp Neurol* 408:365–377.
32. Schulkin J, Gold PW, McEwen BS (1998): Induction of corticotropin-releasing hormone gene expression by glucocorticoids: Implication for understanding the states of fear and anxiety and allostatic load. *Psychoneuroendocrinology* 23:219–243.
33. Owens MJ, Nemeroff CB (1991): Physiology and pharmacology of corticotropin-releasing factor. *Pharmacol Rev* 43:425–472.
34. Takahashi LK (2001): Role of CRF(1) and CRF(2) receptors in fear and anxiety. *Neurosci Biobehav Rev* 25:627–636.
35. Hsu DT, Chen FL, Takahashi LK, Kalin NH (1998): Rapid stress-induced elevations in corticotropin-releasing hormone mRNA in rat central amygdala nucleus and hypothalamic paraventricular nucleus: An in situ hybridization analysis. *Brain Res* 788:305–310.
36. Arborelius L, Owens MJ, Plotsky PM, Nemeroff CB (1999): The role of corticotropin-releasing factor in depression and anxiety disorders. *J Endocrinol* 160:1–12.
37. Hsu DT, Mickey BJ, Langenecker SA, Heitzeg MM, Love TM, Wang H, *et al.* (2012): Variation in the corticotropin-releasing hormone receptor 1 (CRHR1) gene influences fMRI signal responses during emotional stimulus processing. *J Neurosci* 32:3253–3260.
38. Binder EB, Nemeroff CB (2010): The CRF system, stress, depression and anxiety—insights from human genetic studies. *Mol Psychiatry* 15: 574–588.
39. Binder EB, Owens MJ, Liu W, Deveau TC, Rush AJ, Trivedi MH, *et al.* (2010): Association of polymorphisms in genes regulating the corticotropin-releasing factor system with antidepressant treatment response. *Arch Gen Psychiatry* 67:369–379.
40. Smoller JW, Rosenbaum JF, Biederman J, Kennedy J, Dai D, Racette SR, *et al.* (2003): Association of a genetic marker at the corticotropin-releasing hormone locus with behavioral inhibition. *Biol Psychiatry* 54: 1376–1381.
41. Smoller JW, Yamaki LH, Fagermess JA, Biederman J, Racette S, Laird NM, *et al.* (2005): The corticotropin-releasing hormone gene and behavioral inhibition in children at risk for panic disorder. *Biol Psychiatry* 57:1485–1492.
42. Pagliaccio D, Luby JL, Bogdan R, Agrawal A, Gaffrey MS, Belden AC, *et al.* (2014): Stress-system genes and life stress predict cortisol levels and amygdala and hippocampal volumes in children. *Neuropsychopharmacology* 39:1245–1253.
43. Schatzberg AF, Keller J, Tennakoon L, Lembke A, Williams G, Kraemer FB, *et al.* (2014): HPA axis genetic variation, cortisol and psychosis in major depression. *Mol Psychiatry* 19:220–227.
44. Rogers J, Raveendran M, Fawcett GL, Fox AS, Shelton SE, Oler JA, *et al.* (2013): CRHR1 genotypes, neural circuits and the diathesis for anxiety and depression. *Mol Psychiatry* 18:700–707.
45. Pleil KE, Rinker JA, Lowery-Gionta EG, Mazzone CM, McCall NM, Kendra AM, *et al.* (2015): NPY signaling inhibits extended amygdala CRF neurons to suppress binge alcohol drinking. *Nat Neurosci* 18: 545–552.
46. Li XF, Hu MH, Li SY, Geach C, Hikima A, Rose S, *et al.* (2014): Overexpression of corticotropin releasing factor in the central nucleus of the amygdala advances puberty and disrupts reproductive cycles in female rats. *Endocrinology* 155:3934–3944.
47. Toth M, Gresack JE, Bangasser DA, Plona Z, Valentino RJ, Flandreau EI, *et al.* (2014): Forebrain-specific CRF overproduction during development is sufficient to induce enduring anxiety and startle abnormalities in adult mice. *Neuropsychopharmacology* 39:1409–1419.
48. Regev L, Neufeld-Cohen A, Tsoory M, Kuperman Y, Getselter D, Gil S, Chen A (2011): Prolonged and site-specific over-expression of corticotropin-releasing factor reveals differential roles for extended amygdala nuclei in emotional regulation. *Mol Psychiatry* 16:714–728.
49. Keen-Rhinehart E, Michopoulos V, Toufexis DJ, Martin EI, Nair H, Ressler KJ, *et al.* (2009): Continuous expression of corticotropin-releasing factor in the central nucleus of the amygdala emulates the dysregulation of the stress and reproductive axes. *Mol Psychiatry* 14: 37–50.
50. Sink KS, Walker DL, Freeman SM, Flandreau EI, Ressler KJ, Davis M (2013): Effects of continuously enhanced corticotropin releasing factor expression within the bed nucleus of the stria terminalis on conditioned and unconditioned anxiety. *Mol Psychiatry* 18:308–319.
51. Kalin NH, Shelton SE, Davidson RJ (2007): Role of the primate orbitofrontal cortex in mediating anxious temperament. *Biol Psychiatry* 62:1134–1139.
52. Kalin NH, Shelton SE, Davidson RJ, Kelley AE (2001): The primate amygdala mediates acute fear but not the behavioral and physiological components of anxious temperament. *J Neurosci* 21:2067–2074.
53. Clark JD, Gebhart GF, Gonder JC, Keeling ME, Kohn DF (1997): Special Report: The 1996 Guide for the Care and Use of Laboratory Animals. *ILAR J* 38:41–48.
54. Emborg ME, Joers V, Fisher R, Brunner K, Carter V, Ross C, *et al.* (2010): Intraoperative intracerebral MRI-guided navigation for accurate targeting in nonhuman primates. *Cell Transplant* 19:1587–1597.
55. Emborg ME, Hurley SA, Joers V, Tromp do PM, Swanson CR, Ohshima-Hosoyama S, *et al.* (2014): Titer and product affect the distribution of gene expression after intraputamenal convection-enhanced delivery. *Stereotact Funct Neurosurg* 92:182–194.
56. Truwit CL, Liu H (2001): Prospective stereotaxy: A novel method of trajectory alignment using real-time image guidance. *J Magn Reson Imaging* 13:452–457.
57. Brodsky EK, Block WF, Alexander AL, Emborg ME, Ross CD, Sillay KA (2011): Intraoperative device targeting using real-time MRI. In: *Proceedings of the IEEE Biomedical Sciences and Engineering Conference: Image Informatics and Analytics in Biomedicine*, Bsec 2011. Piscataway, NJ: Institute of Electronics and Electrical Engineers.
58. Grabow B, Block W, Alexander AL, Hurley S, CDR, Sillay K, *et al.* (2012): Extensible real-time MRI platform for intraoperative targeting and monitoring. Poster presentation #1585 at the International Society for Magnetic Resonance in Medicine 20th Annual Scientific Meeting and Exhibition, May 5–11, Melbourne, Australia.
59. Grabow BP, Oler JA, Riedel M, Fekete EM, Kovner R, brodsky EK, *et al.* (2014): Alteration of molecular neurochemistry: MRI-guided delivery of viral vectors to the primate amygdala. Oral presentation #672 at The International Society for Magnetic Resonance in Medicine and the European Society for Magnetic Resonance in Medicine and Biology Joint Annual Scientific Meeting and Exhibition, May 10–16, Milan, Italy.
60. Brady ML, Raghavan R, Block W, Grabow B, Ross C, Kubota K, *et al.* (2015): The relation between catheter occlusion and backflow during intraparenchymal cerebral infusions. *Stereotact Funct Neurosurg* 93: 102–109.
61. Amaral DG, Bassett JL (1989): Cholinergic innervation of the monkey amygdala: An immunohistochemical analysis with antisera to choline acetyltransferase. *J Comp Neurol* 281:337–361.
62. Van Pett K, Viau V, Bittencourt JC, Chan RK, Li HY, Arias C, *et al.* (2000): Distribution of mRNAs encoding CRF receptors in brain and pituitary of rat and mouse. *J Comp Neurol* 428:191–212.
63. Liang KC, Lee EHY (1988): Intra-amygdala injections of corticotropin releasing factor facilitate inhibitory avoidance learning and reduce exploratory behavior in rats. *Psychopharmacology (Berl)* 96:232–236.
64. Sajdyk TJ, Schober DA, Gehlert DR, Shekhar A (1999): Role of corticotropin-releasing factor and urocortin within the basolateral

- amygdala of rats in anxiety and panic responses. *Behav Brain Res* 100:207–215.
65. Tazi A, Dantzer R, LeMoal M, Rivier J, Vale W, Koob GF (1987): Corticotropin-releasing factor antagonist blocks stress-induced fighting in rats. *Regul Pept* 18:37–42.
 66. Heinrichs SC, Pich EM, Miczek KA, Britton KT, Koob GF (1992): Corticotropin-releasing factor antagonist reduces emotionality in socially defeated rats via direct neurotropic action. *Brain Res* 581:190–197.
 67. Rainnie DG, Bergeron R, Sajdyk TJ, Patil M, Gehlert DR, Shekhar A (2004): Corticotropin releasing factor-induced synaptic plasticity in the amygdala translates stress into emotional disorders. *J Neurosci* 24:3471–3479.
 68. Sajdyk TJ, Gehlert DR (2000): Astressin, a corticotropin releasing factor antagonist, reverses the anxiogenic effects of urocortin when administered into the basolateral amygdala. *Brain Res* 877:226–234.
 69. Jochman KA, Newman SM, Kalin NH, Bakshi VP (2005): Corticotropin-releasing factor-1 receptors in the basolateral amygdala mediate stress-induced anorexia. *Behav Neurosci* 119:1448–1458.
 70. Koob GF, Heinrichs SC (1999): A role for corticotropin releasing factor and urocortin in behavioral responses to stressors. *Brain Res* 848: 141–152.
 71. Justice NJ, Yuan ZF, Sawchenko PE, Vale W (2008): Type 1 corticotropin-releasing factor receptor expression reported in BAC transgenic mice: Implications for reconciling ligand-receptor mismatch in the central corticotropin-releasing factor system. *J Comp Neurol* 511:479–496.
 72. Swiergiel AH, Takahashi LK, Kalin NH (1993): Attenuation of stress-induced behavior by antagonism of corticotropin-releasing factor receptors in the central amygdala in the rat. *Brain Res* 623:229–234.
 73. Bakshi VP, Kalin NH (2000): Corticotropin-releasing hormone and animal models of anxiety: Gene-environment interactions. *Biol Psychiatry* 48:1175–1198.
 74. Kalin NH, Shelton SE, Kraemer GW, McKinney WT (1983): Corticotropin-releasing factor administered intraventricularly to rhesus monkeys. *Peptides* 4:217–220.
 75. Chalmers DT, Lovenberg TW, De Souza EB (1995): Localization of novel corticotropin-releasing factor receptor (CRF2) mRNA expression to specific subcortical nuclei in rat brain: Comparison with CRF1 receptor mRNA expression. *J Neurosci* 15:6340–6350.
 76. Rominger DH, Rominger CM, Fitzgerald LW, Grzanna R, Largent BL, Zaczek R (1998): Characterization of [¹²⁵I]saunavagine binding to CRH2 receptors: Membrane homogenate and autoradiographic studies. *J Pharmacol Exp Ther* 286:459–468.
 77. Strome EM, Wheler GH, Higley JD, Loriaux DL, Suomi SJ, Doudet DJ (2002): Intracerebroventricular corticotropin-releasing factor increases limbic glucose metabolism and has social context-dependent behavioral effects in nonhuman primates. *Proc Natl Acad Sci U S A* 99: 15749–15754.
 78. Kalin NH, Shelton SE, Davidson RJ (2000): Cerebrospinal fluid corticotropin-releasing hormone levels are elevated in monkeys with patterns of brain activity associated with fearful temperament. *Biol Psychiatry* 47:579–585.
 79. Nemeroff CB, Widerlov E, Bissette G, Walleus H, Karlsson I, Eklund K, *et al.* (1984): Elevated concentrations of CSF corticotropin-releasing factor-like immunoreactivity in depressed patients. *Science* 226: 1342–1344.
 80. Austin MC, Janosky JE, Murphy HA (2003): Increased corticotropin-releasing hormone immunoreactivity in monoamine-containing pontine nuclei of depressed suicide men. *Mol Psychiatry* 8:324–332.
 81. Hiroi N, Wong ML, Licinio J, Park C, Young M, Gold PW, *et al.* (2001): Expression of corticotropin releasing hormone receptors type I and type II mRNA in suicide victims and controls. *Mol Psychiatry* 6: 540–546.
 82. Merali Z, Du L, Hrdina P, Palkovits M, Faludi G, Poulter MO, Anisman H (2004): Dysregulation in the suicide brain: mRNA expression of corticotropin-releasing hormone receptors and GABA(A) receptor subunits in frontal cortical brain region. *J Neurosci* 24:1478–1485.
 83. Merali Z, Kent P, Du L, Hrdina P, Palkovits M, Faludi G, *et al.* (2006): Corticotropin-releasing hormone, arginine vasopressin, gastrin-releasing peptide, and neuromedin B alterations in stress-relevant brain regions of suicides and control subjects. *Biol Psychiatry* 59: 594–602.
 84. Raadsheer FC, van Heerikhuizen JJ, Lucassen PJ, Hoogendijk WJ, Tilders FJ, Swaab DF (1995): Corticotropin-releasing hormone mRNA levels in the paraventricular nucleus of patients with Alzheimer's disease and depression. *Am J Psychiatry* 152:1372–1376.
 85. Flandreau EI, Ressler KJ, Owens MJ, Nemeroff CB (2012): Chronic overexpression of corticotropin-releasing factor from the central amygdala produces HPA axis hyperactivity and behavioral anxiety associated with gene-expression changes in the hippocampus and paraventricular nucleus of the hypothalamus. *Psychoneuroendocrinology* 37:27–38.
 86. Regev L, Tsoory M, Gil S, Chen A (2012): Site-specific genetic manipulation of amygdala corticotropin-releasing factor reveals its imperative role in mediating behavioral response to challenge. *Biol Psychiatry* 71:317–326.
 87. Ghashghaee HT, Hilgetag CC, Barbas H (2007): Sequence of information processing for emotions based on the anatomic dialogue between prefrontal cortex and amygdala. *Neuroimage* 34:905–923.
 88. Kostich WA, Grzanna R, Lu NZ, Largent BL (2004): Immunohistochemical visualization of corticotropin-releasing factor type 1 (CRF1) receptors in monkey brain. *J Comp Neurol* 478:111–125.
 89. Foote SL, Cha CI (1988): Distribution of corticotropin-releasing-factor-like immunoreactivity in brainstem of two monkey species (*Saimiri sciureus* and *Macaca fascicularis*): An immunohistochemical study. *J Comp Neurol* 276:239–264.
 90. Amaral DG, Price JL, Pitkänen A, Carmichael ST (1992): Anatomical organization of the primate amygdaloid complex. In: Aggelton JP, editor. *The Amygdala: Neurobiological Aspects of Emotion, Memory, and Mental Dysfunction*. New York: Wiley-Liss, 1–66.
 91. Price JL, Amaral DG (1981): An autoradiographic study of the projections of the central nucleus of the monkey amygdala. *J Neurosci* 1:1242–1259.
 92. Ray JP, Price JL (1993): The organization of projections from the mediodorsal nucleus of the thalamus to orbital and medial prefrontal cortex in macaque monkeys. *J Comp Neurol* 337:1–31.
 93. Bale TL, Vale WW (2004): CRF and CRF receptors: Role in stress responsiveness and other behaviors. *Annu Rev Pharmacol Toxicol* 44: 525–557.
 94. Koob GF, Zorrilla EP (2012): Update on corticotropin-releasing factor pharmacotherapy for psychiatric disorders: A revisionist view. *Neuropsychopharmacology* 37:308–309.
 95. Coric V, Feldman HH, Oren DA, Shekhar A, Pultz J, Dockens RC, *et al.* (2010): Multicenter, randomized, double-blind, active comparator and placebo-controlled trial of a corticotropin-releasing factor receptor-1 antagonist in generalized anxiety disorder. *Depress Anxiety* 27: 417–425.
 96. Zobel AW, Nickel T, Kunzel HE, Ackl N, Sonntag A, Ising M, Holsboer F (2000): Effects of the high-affinity corticotropin-releasing hormone receptor 1 antagonist R121919 in major depression: The first 20 patients treated. *J Psychiatr Res* 34:171–181.
 97. Binneman B, Feltner D, Kolluri S, Shi Y, Qiu R, Stiger T (2008): A 6-week randomized, placebo-controlled trial of CP-316,311 (a selective CRH1 antagonist) in the treatment of major depression. *Am J Psychiatry* 165:617–620.
 98. O'Rourke H, Fudge JL (2006): Distribution of serotonin transporter labeled fibers in amygdaloid subregions: Implications for mood disorders. *Biol Psychiatry* 60:479–490.
 99. Paxinos G, Huang X, Petrides M, Toga A (2009): *The Rhesus Monkey Brain in Stereotaxic Coordinates*, 2nd ed San Diego: Academic Press.

Overexpressing Corticotropin-Releasing Hormone in the Primate Amygdala Increases Anxious Temperament and Alters Its Neural Circuit

Supplemental Information

SUPPLEMENTAL METHODS AND RESULTS

Visualization of Endogenous CRH Expressing Neurons

To identify Ce neurons that endogenously express CRH (see **Figure 1E** in the main manuscript), tissue sections (40 μ m) through the amygdala from one cynomolgus monkey (*Macaca fascicularis*) were stained for NeuN and CRH. To aid in localization of the Ce, sections were first incubated with a somatostatin primary antibody raised in goat (catalog #sc-7819; Santa Cruz Biotechnology, Dallas, TX) followed by secondary antibody (Alexa Fluor 568 donkey anti-goat; Life Technologies). Sections were then incubated in NeuN primary antibody raised in mouse (catalog #MAB377; Millipore, Billerica, MA), followed by a fluorescently-labeled secondary antibody (Alexa Fluor 647 donkey anti-mouse; Life Technologies). Sections were washed and treated with an avidin/biotin blocking kit (Vector Laboratories) and CRH-expressing neurons were then double-labeled using a CRH antibody raised in guinea pig (catalog # T-5007; Peninsula Labs, San Carlos, CA) to allow for double labeling. Sections were then treated with secondary antibody (biotinylated goat anti-guinea pig, Vector Laboratories) followed by incubation with streptavidin-conjugated Alexa Fluor 488 (Life Technologies, Grand Island, NY). CRH signal was amplified with a biotinylated anti-streptavidin antibody (Vector Laboratories, Burlingame, CA) followed again by incubation with streptavidin-conjugated Alexa Fluor 488. To dampen the autofluorescence signal, tissue was then treated with the autofluorescence eliminator reagent (EMD Millipore, Billerica, MA). Finally, sections were mounted and cover slipped using ProLong Gold (Life Technologies) and slides were visualized with an A1R confocal microscope (Nikon, Melville, NY) at 20x magnification. Edges of the lateral division of the Ce were identified using the stain for somatostatin.

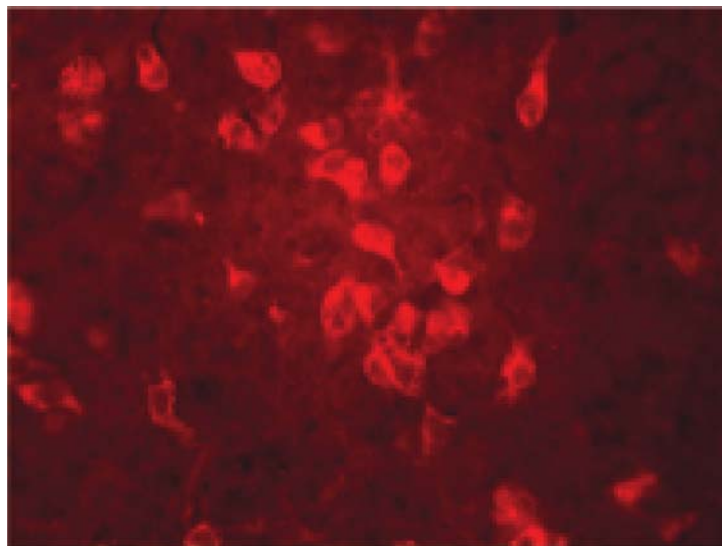
Development and Validation of CRH Viral Vector Construct

The DNA sequence corresponding to the entire open reading frame of rhesus prepro-CRH (GenBank accession #XM_001094433.2; bases 327 – 971) was inserted into the AAV2-MCS plasmid (Vector Biolabs, Philadelphia, PA). Expression of CRH from this plasmid was under control of the CMV promoter. In addition, the AAV2-MCS plasmid is thought to enhance expression by inserting an unrelated intronic intervening sequence upstream of the CRH sequence that is spliced out during processing to the mature mRNA.

The effectiveness of the plasmid at directing CRH expression was demonstrated by transfecting HEK-293 cells, followed by immunocytochemical detection of CRH expression using a commercially available CRH antibody produced in rabbit (T-4037; Bachem), followed by a fluorescently-labeled Alexa Fluor 568 conjugated goat anti-rabbit secondary antibody (Life Technologies, Grand Island, NY). CRH immunoreactivity was readily detected in the HEK-293 cells transfected cells (see Figure S1). The plasmid sequence was then packaged into AAV2 at a titer of 3.1×10^{13} genome copies/ml (Vector Biolabs).

In Vivo Validation of CRH Overexpression in a Pilot Cynomolgus Monkey

Using the methods described in the paper and detailed below, the effectiveness of the CRH AAV2 virus to direct CRH over expression in vivo was first demonstrated in a pilot monkey. For this study, 12 μ l of the virus solution was infused into two separate locations within the amygdala of a cynomolgus monkey (*Macaca fascicularis*). In this pilot animal, the RT-IMRI along with the postmortem analysis revealed that the major



CRH transfected cells *in vitro*

Figure S1. Immunocytochemical detection of CRH expression in HEK293 cells transfected with a plasmid directing expression of CRH.

locus of infection was in the dorsal part of the basal nucleus, which is directly ventral to the Ce. In addition to establishing infusion parameters, this pilot animal allowed us to refine the targeting procedure. The animal was sacrificed 5 weeks following injection and was perfused with 0.9% heparinized-saline followed by 4% paraformaldehyde (PFA) in phosphate-buffered saline (PBS), pH 7.4. After overnight fixation in 4% PFA, the brain was cut into 14 mm thick slabs, cryoprotected in 20% sucrose/5% glycerol and 40 μ m frozen sections were cut through the amygdala on a cryostat (CM3050, Leica Biosystems, Buffalo Grove, IL).

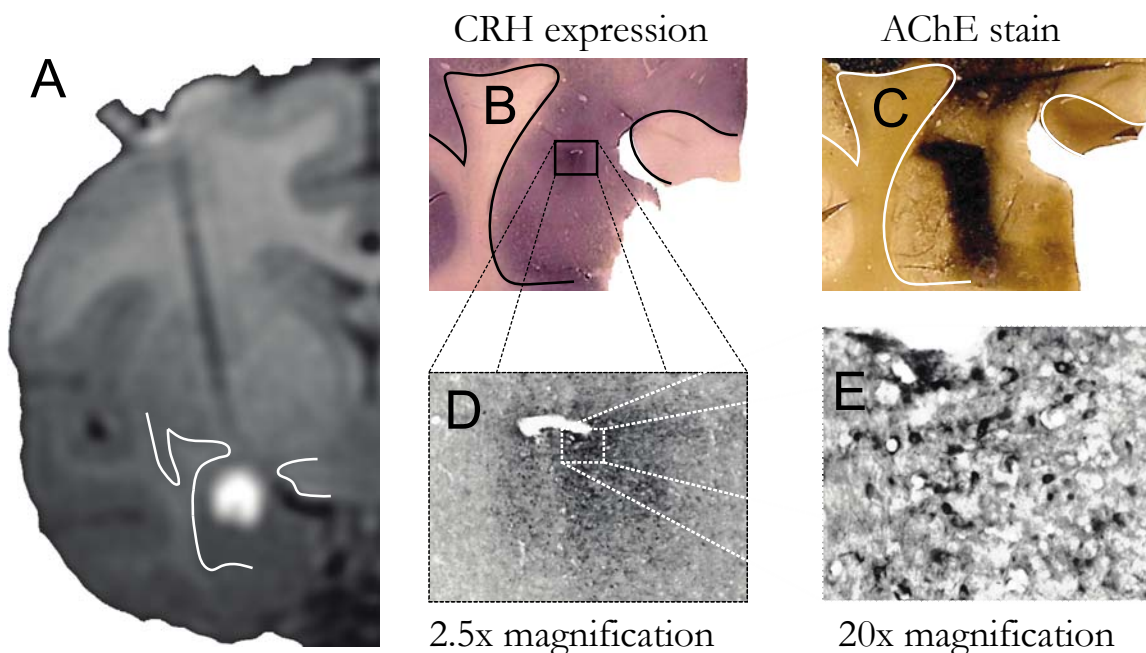


Figure S2. RT-IMRI guided infusion of CRH viral vector effectively guides overexpression of CRH in the amygdala. In this pilot animal, the dorsal part of the basal nucleus was the primary region infected. **(A)** Infusion location was verified using real-time imaging by adding gadolinium into the viral vector solution. **(B)** CRH expression was verified by staining for CRH. **(C)** AChE staining in a slide adjacent to the CRH section was used to determine the location of amygdalar nuclei. **(D & E)** CRF overexpression at 2.5x, and 20x magnification, respectively.

Sections were processed for immunohistochemistry with the same CRH antibody used in the *in vitro* studies. Signal was visualized with goat anti-rabbit biotinylated secondary antibody (Vector Laboratories; Burlingame, CA) using diaminobenzene as the chromogen. Acetylcholinesterase (AChE) staining was used to identify the structural

details of the amygdala nuclei (1). The method was based on a previously published procedure (2). Immunohistochemical examination of the brain from the pilot animal demonstrated that viral vector containing the CRH construct used with the optimized perfusion parameters effectively increased CRH expression in the infused region of the amygdala (Figure S2).

Assessing Behavior and Cortisol as Components of AT

A trained rater, who was blind to monkey group assignment, scored the animals' behavior during the no eye contact condition of the human intruder paradigm (NEC). Freezing was defined as a lack of movement for greater than 3-seconds, and was recorded in seconds per 5-minutes of NEC exposure. Mean freezing scores were log-transformed and standardized after covarying for age and sex. Cooing was measured as the number of coo-vocalizations during each 5-min period of NEC-exposure. Mean cooing frequencies were square-root transformed, and standardized after removing the effects of age and sex. Plasma cortisol ($\mu\text{g}/\text{dL}$) was quantified based on samples taken immediately after NEC-exposure. Cortisol was quantified in duplicate using the DPC Coat-a-count radioimmunoassay (Siemens, Los Angeles, CA). Cortisol values were standardized after removing any effects of age, sex, and the time-of-day in which samples were taken. A composite measure of AT (3, 4) was computed as the combination of standardized freezing, cooing and cortisol measures, as in $(Z_{\text{freezing}} - Z_{\text{cooing}} + Z_{\text{cortisol}}) / 3$. Further details on the validation and methods used to assess AT have been previously described (3, 5, 6).

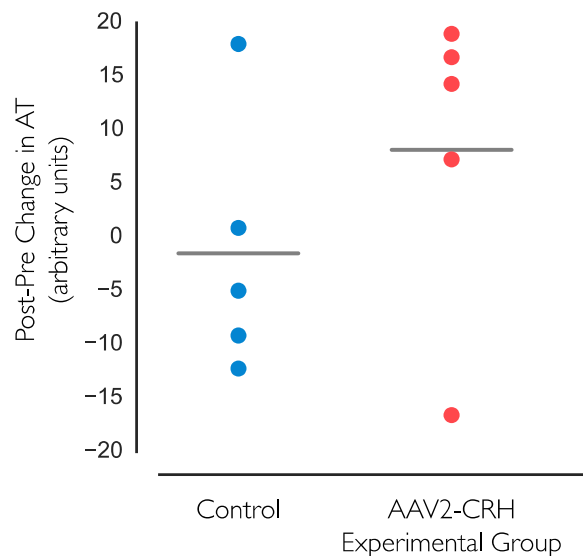


Figure S3. Compared to controls the CRH overexpressing animals demonstrated a significant increase in AT (unpaired between-groups $t = 2.040$, $p = 0.0405$, one-tailed). Note that the data are plotted without residualizing for the effect for age.

Placement of the Trajectory Guide Base

Before the procedure, the animals were anesthetized with ketamine (up to 20 mg/kg, intramuscular (IM)), prepared for surgery, and then placed in a magnetic resonance imaging (MRI)-compatible stereotaxic frame. The animals were intubated and received isoflurane anesthesia (1–3%, intratracheal). Atropine sulfate (0.01-0.3 mg/kg, IM) was administered to depress salivary secretion, and buprenorphine (0.01-0.03 mg/kg, IM) was given for analgesia. To maintain fluids and electrolytes, Plasmalyte (up to 10 mg/kg/h, intravenous (IV)) was administered. Cefazolin (20-25 mg/kg, IM or IV) was administered as a prophylactic antibiotic one day prior to the surgery. Cefazolin was also administered immediately prior to surgery, and then every 6 hours while under anesthesia. All drugs and treatments were given in consultation with veterinary staff. Vital signs (heart rate, respiration, oxygen saturation, and CO₂) were continuously monitored. Body temperature was monitored during the surgical procedure and maintained by wrapping the animals for warmth. To reduce intracranial pressure and prevent brain swelling, mannitol (up to 2.0 g/kg, IV) was given as needed. Cefazolin (20-25 mg/kg, IM or IV) or cephalexin (20-25 mg/kg, oral) was given twice daily for five days after surgery to prevent infection. The animals were allowed to recover and testing did not commence before 2 months after surgery.

Placement of the MRI-compatible trajectory guide bases followed previously reported methods (see refs (7, 8) for details) modified for Ce targeting. Prior to surgery the 3D T1W MRIs were used to visualize Ce in three planes (sagittal, axial, and coronal) and identify the entry point for the catheter. The anteroposterior zero plane was identified by visualization of the ear canals. The dorsoventral zero was defined as the surface of the brain at the site of insertion and the mediolateral zero was defined as the middle of the sagittal sinus. Based on the three sets of images a target point in the Ce was determined and a trajectory was planned to define the location of the entry at the skull (see Figure 2A in the main manuscript). The distance from entry point to target was calculated based on the zero coordinates previously defined, using GE MRI software. Intraoperative MRI guidance of the catheter was performed using a pivot point-based MRI compatible external trajectory guide (Navigus brain port, Medtronic Inc., Minneapolis, MN, see Figure 2B in the main manuscript). Modifications were made

to this system to adapt it for the placement of catheters by the addition of a guiding insert, a customized base to fit the nonhuman primate skull and the addition of a laser alignment pointer that fastens to a micromanipulator. Placement of the MRI-compatible trajectory guide bases was performed in the surgical suite (adjacent to the MRI suite) under sterile conditions. Using stereotactic guidance, 11-12 mm in diameter craniotomies were performed bilaterally at the planned entry points. Each trajectory guide base was mounted on the skull over the craniotomy with three titanium AutoDrive self-tapping screws (OsteoMed, Addison, TX) and dental acrylic. Surgical gelfoam that was moistened with sterile saline was placed over the craniotomies and the bases were capped with sterile plastic base plugs (Navigus).

Catheter Trajectory Planning and Insertion

The animals were transported from the surgical suite to the MRI suite under anesthesia. Sterile conditions were maintained in the MRI suite during viral vector delivery. A 3-inch circular surface coil (MR Instruments, Minneapolis, MN) was positioned above the animal's head, transverse to the main magnetic field, with the Navigus brain port located near the center of the coil. A sterile MR-visible alignment guide was inserted into the trajectory guide base. A high-resolution, volumetric roadmap scan was acquired for later target identification using a 3D IR GRE MRI with a 12° flip angle, 256 x 224 x 248 acquisition matrix (0.35 x 0.35 x 0.80 mm voxels), 9.1/3.9 ms repetition time/echo time (TR/TE), 450 ms inversion time (TI), 97 Hz/pixel receiver bandwidth, 6.5 minute total acquisition time. The targeting was performed using a platform for real-time MR-guided prospective stereotaxy (9) that was initially developed by the University of Wisconsin (10-13).

The brain port consists of a MR-visible fluid-filled alignment guide seated in a ball-and-socket pivot joint with two degrees of rotational freedom. The base constrains the guide such that its proximal tip passes the center of the pivot joint, and the distal end up the guide extends away from the skull. After identifying the desired target point in the brain and the location of the pivot point in the high-resolution 3D T1-weighted "roadmap" volume, the prospective stereotaxy tool calculates an "aiming point" outside the skull that is co-linear with the target and alignment guide pivot points and then

performs real-time imaging (2D GRE, 384 x 384 acquisition matrix size, 1 mm slice thickness, 0.52 mm in-plane resolution, 25° flip angle, TR = 16 ms, 650 Hz/pixel receiver bandwidth, 6 s/frame) of a plane perpendicular to and centered on the aiming point, allowing the operator to move the alignment guide until its image overlaps with the software-displayed aiming point. Once the alignment guide is in position, the base is locked into place and the catheter can be inserted.

This system is built on top of the RTHawk scanner interface (HeartVista, Palo Alto, CA), which permits the implementation of image-guided interventional procedures (14), and the VURTIGO toolkit (Visual Understanding of Real-Time Image Guided Operations, Sunnybrook Health Sciences Centre; Toronto, Canada), an open-source visualization platform that allows simultaneous display and interaction with multiple 3D and 2D datasets (15). The platform allows the surgeon to align the brain ports used to orient catheters with real-time feedback in an interactive manner (see Figure 2C in the main manuscript).

When the trajectory angle (anteroposterior, mediolateral direction) of the fluid-filled alignment guide was confirmed to be on target, the alignment stem was locked into position. The fluid-filled alignment guide was removed, the remote introducer (Navigus) was fastened to the stem, and the guiding insert was placed in the alignment stem. The catheter for the infusion was threaded through the remote introducer and the guiding insert, and was fastened to the remote introducer by a locking mechanism. FEP Teflon infusion lines (IDEX Health & Science, Oak Harbor, WA) were used to connect the catheter via a pressure sensor transducer to a 100 µl Hamilton syringe (Hamilton Company USA, Reno, NV) that was placed in a MRI-compatible syringe pump attached to the control mechanism of a standard Harvard apparatus PHD 2000 (Holliston, MA). Monitoring of the pressure in the infusion line was performed using the infusion pump controller system (Engineering Resources Group, Inc., Pembroke Pines, FL). A computer was connected to the pump controller for infusion protocol programming, and connected to a pressure sensor transducer to monitor infusion line pressure at the pump output port. The infusion line was primed with a loading line solution (Dulbecco's phosphate-buffered saline (D-PBS) without Ca^{2+} and Mg^{2+} with 5% glycerol) and the catheter was loaded with the viral vector containing the CRH construct and Gd. After

pressure in the line was stabilized, the catheter was introduced into the brain, advancing the remote introducer at approximately 10-15 mm/minute. The catheter was advanced two-thirds of the measured depth towards the target for partial insertion, and another targeting 3D T1W MRI was performed to confirm the correct trajectory, and calculate the remaining distance from catheter tip to target (see Figure 2D in the main manuscript). Once confirmed, the catheter was advanced to its final position and the stylet was slowly retracted. When the pressure reading on the infusion pump controller system stabilized, the infusion began.

Real-time scan control and visualization was conducted on a high-performance external workstation with two quad-core Intel Xeon E5620, 2.4 GHz CPUs, 12 GB of memory, an NVIDIA GF100 Quadro 4000 graphics card, and dual gigabit Ethernet controllers, running 64-bit Linux. Scanner interface was via an internal Ethernet switch. Visualization display was available on a screen in the control room, which was placed in the scanner room window so that an operator could lean into the bore and reposition the MR-visible fluid-filled alignment guide to the optimal trajectory angle.

The catheter (100 mm Valve Tip Catheter, Engineering Resources Group, Inc., Pembroke Pines, FL) was a fused silica cannula with a polyimide tubing tip and was sealed with a retractable glass fiber stylet. Its dimensions were: tip—outer diameter (OD) = 0.40 mm, inner diameter (ID) = 0.345 mm, length = 3.0 mm; shaft—OD = 0.67 mm, ID = 0.45 mm, length = 97.0 mm from ferrule, stylet OD = 0.275 mm.

Different imaging sequences were performed during and immediately following the infusion depending on the intended monitoring goal. For rapid, qualitative monitoring of infusion progression, a time series of images of a single coronal slice containing the target and catheter/infusion track was acquired. The acquisition used a 2D SPGR sequence with 256 x 192 matrix size over a 140 mm field of view (FOV), for a resolution of 0.55 x 0.73 mm. The imaging used a slice thickness of 2.5 mm, TR/TE of 33.0/3.8 ms with two signal averages, flip angle of 50°, and a receiver bandwidth of 244 Hz/pixel. This sequence provides primarily infusate/anatomy contrast and allowed for early verification that the infusion was on target and that the infusion was not experiencing significant backflow along the catheter. For a qualitative visualization of the volumetric infusate delivery region, the previously described 3D roadmap was reacquired. This

sequence provides sensitivity to the contrast-enhanced infusate and sufficient gray/white contrast for easy identification of the infusion's anatomical location.

The infusate consisted of AAV2-CRH vector in a solution of D-PBS without Ca^{2+} and Mg^{2+} with 5% glycerol. To facilitate *in vivo* MRI visualization of the infusion, Gd was mixed with the viral vector to reach final concentration 0.66 mM (see Figure 2E in the main manuscript). A total volume of 12 μl was infused at a steady rate of 1 $\mu\text{l}/\text{min}$ per infusion site, for a total of 24 μl per hemisphere. After each infusion the catheter was removed, and after all infusions were complete the animal was transported back to the surgical suite and the craniotomies were closed in layers.

Details Regarding Imaging Methods

All behavioral (NEC) and brain imaging (FDG-PET, fMRI, and DTI) measures were assessed twice, once before surgery and again approximately 2 months later in the 5 CRH-overexpressing monkeys, and at similar intervals in their 5 matched unoperated controls.

Measuring Glucose Metabolism Using [^{18}F]Deoxyglucose PET

Subjects were exposed to the NEC-context for 30 minutes. Immediately prior to NEC exposure, subjects were restrained in a squeeze cage and received an intravenous injection of FDG. Thus, FDG-uptake occurred in metabolically active cells while animals freely behaved in the NEC context. Following 30-minute exposure to the NEC-context, subjects were anesthetized with a 15 mg/kg intramuscular injection of ketamine, and plasma was collected for quantifying cortisol. The animals were intubated and placed in the PET scanner while anesthesia was maintained using 1-3% isoflurane gas. FDG and attenuation scans were acquired using a Siemens Focus 220 microPET scanner. Images were reconstructed using standard filtered-backprojection techniques with attenuation- and scatter-correction. This technique results in FDG-PET scans that represent the integrated brain metabolism throughout each NEC-exposure. FDG-PET images were transformed to standard space as described below, and intensity-normalized with SPAMALIZE (http://psyphz.psych.wisc.edu/~oakes/spam/spam_frames.htm) so that the mean brain

value was equivalent across individuals. Each animal's FDG-PET images were aligned to the corresponding pre/post T1-anatomical image using a rigid body mutual information warp, and the transformation from T1 to template-space (described below) was then applied to the FDG-PET image. A 6 mm FWHM Gaussian smoothing kernel was applied to account for individual differences in brain anatomy and registration.

MRI Acquisition and Analysis

Prior to MRI acquisition, the monkeys were anesthetized with ketamine (15 mg/kg, IM). The animals were placed in a MRI-compatible stereotaxic frame, administered dexmedetomidine (0.015 mg/kg, IM), and scanned for approximately one hour. Heart rate and oxygen saturation were monitored throughout the scan. Ketamine (up to 5 mg/kg, IM) was repeated as needed approximately every 20-40 minutes throughout the scan. At the end of the scan the dexmedetomidine was reversed with atipamezole (0.15 mg/kg, IM) and animals were removed from the scanner and monitored until they fully recovered from anesthesia.

All imaging was performed in a 3-Tesla GE 750 (GE Healthcare; Waukesha, WI) MRI scanner with a HD T/R Quad extremity coil (Invivo Corp, Gainesville, FL). The head was fixed in the sphinx position using a custom stereotaxic frame that fit inside the coil. Whole-brain anatomical images were acquired using an axial T1-weighted 3D inversion recovery prepared fast spoiled gradient recalled scan (TI = 600 ms, TR = 11.45 ms, TE = 5.4 ms, flip angle $\alpha = 10^\circ$, number of excitations [NEX] = 2, FOV = 140 x 140 mm, matrix = 512 x 512, in-plane resolution = 0.27 mm, slice thickness/gap = 0.5/0 mm, 248 slices). Resting-state functional MRI's were acquired using an echo planar imaging sequence (EPI; TR/TE = 2000/25 ms, $\alpha = 90^\circ$, NEX = 1, FOV = 140 x 140 mm, matrix = 64 x 64, in-plane resolution = 2.19 mm, slice thickness/gap = 3.1/0.5 mm, 26 interleaved slices). Diffusion weighted imaging was performed using a two-dimensional, echo-planar, spin-echo sequence (TR/TE = 10000/85.3 ms, NEX = 1, FOV = 144 x 144 mm, matrix = 256 x 256, in-plane voxel dimension = 0.56 x 0.56 mm², slice thickness/gap = 1.3/0 mm, 68 interleaved slices, echo-planar spacing = 816 μ s). Diffusion-weighted imaging ($b = 1000$ s/mm²) was performed in 72 non-collinear directions with 6 non-diffusion weighted images. Images were acquired in the coronal plane through the

entire monkey brain. A co-planar field map was also obtained using a gradient echo with images at two echo times: TE1 = 7 ms, TE2 = 10 ms.

Study-Specific Template Creation and Individual-Subject Registration

All pre-processing was performed using well-established methods for rhesus neuroimaging data (3, 5, 16-21). Prior to spatial normalization, T1 images were manually segmented into brain and non-brain tissue using SPAMALIZE. T1-brain images were then transformed to standard space (methods described below), and transformation parameters were saved. Study-specific T1-anatomical template creation was performed using an iterative procedure using Advanced Normalization Tools (ANTS; <http://sourceforge.net/projects/advants>; (22, 23)). First, each subject's two T1-anatomical images were aligned to each other, and averaged to create a subject-specific average. Then, each subject's T1-anatomical average was aligned using a non-linear symmetric diffeomorphic image registration in ANTS to a predefined template-space (18) that was created from 592 T1-MRI images from young rhesus monkeys. Nonlinear registration was performed using a symmetric diffeomorphic image registration and a .25 gradient step-size; a pure cross correlation cost-function with window radius 2 and weight 1; the similarity matrix was smoothed with sigma = 2; and this process was repeated at 4 increasingly fine levels of resolution with 30, 20, 20, and 5 iterations at each level respectively. The average of T1's in 'standard-space' was computed and taken to be the study-mean. Similarly, the non-linear deformation-field was also averaged and taken to be the deformation-mean. The deformation-mean was inverted and 15% of this deformation was applied to the study-mean, to obtain the first iteration of the study-specific template. To maintain comparability to other studies, and to printed brain atlases, the affine transformation was *not* inverted and applied to the study-mean. The same procedure was performed aligning each subject's T1-anatomical images to the initial study-specific template. After averaging the images and deformations, a new study-specific template was created by applying 15% of the newest mean-deformation to the newest study-mean. This process was repeated 4 times, to obtain a final study-specific template. Each subject's original T1-anatomical images were then aligned to this study-specific template by combining the subject-specific and

study-specific deformations. This procedure resulted in T1 images in standard space, along with corresponding deformations that could be applied to other modalities.

fMRI Analytic Methods

Intrinsic functional connectivity was assessed with previously published methods (16, 20). fMRI scans were performed using methods modified from prior work demonstrating the reliability of collecting resting fMRI data in anesthetized rhesus monkeys (24). All fMRI processing steps were carried out in AFNI (25), unless otherwise indicated. Resting state scans were slice timing and motion corrected, had the first 4 frames removed, and were adjusted for field inhomogeneities with a field map correction. The preprocessed resting state scans were aligned to standard space using the deformations derived from the anatomical scans. In order to reduce the influence of non-neuronal fluctuations on functional connectivity estimates, average signal intensity time courses from the white matter and cerebrospinal fluid were regressed out of the EPI time series (26). The residualized resting state signal was further processed with a temporal bandpass filtering (low = 0.01 Hz, high = 0.1 Hz).

We employed a standard a priori seed-based approach to quantifying group differences in intrinsic functional connectivity. The seed region was defined as the conjunction of the overlapping gadolinium infusion area within the dorsal amygdala (see yellow region in Figure 3E in the main manuscript), and the region of dorsal amygdala demonstrating significant CRH-induced change in brain metabolism (see Figure 6A in the main manuscript). For each subject, the BOLD time series was averaged across the voxels defining the seed, and a voxelwise temporal correlation between the extracted EPI time-series and the times-series throughout the rest of the brain was performed. Correlation maps were normalized (Fisher's *r*-to-*z* transformation) and spatially blurred with a 6 mm FWHM Gaussian smoothing kernel. These images were used in voxelwise analyses to identify AAV2-CRH associated alterations in dorsal amygdala functional connectivity as described in the statistical analyses section below.

DTI Analytic Methods

DTI analysis included distortion corrections using FSL's tools for eddy and field distortions (27). Tensors were estimated using a robust estimation of tensors by outlier rejection (RESTORE, as implemented in Camino software; (28)). This method has been proven to increase reliability of the tensor estimation (29). Because standard intensity-based registration based on the T1-anatomical images does not preserve tensor orientation, tensor images were normalized using a high-dimensional registration method that incorporates the tensor orientation (DTI-TK (30)). This procedure is nearly identical to the iterative ANTS-procedure described above, with the exception that the alignment between scans was determined based on the tensor orientation as opposed to image intensity. The result of this procedure was a study-specific tensor-based template based on multiple registration iterations, and corresponding study-specific template-space tensor images for each scan. To ensure that DTI data were in the same space as other neuroimaging modalities, a final rigid-body transformation was performed to align the study-specific DTI template with the study-specific T1 template, and this transformation was applied to individual images to obtain standard-space tensor images. The resulting standard-space DTI images were used to quantify the local diffusion parameters: fractional anisotropy (FA), mean diffusivity (MD), axial diffusivity (AD) and radial diffusivity (RD). Images were smoothed with a 6 mm FWHM Gaussian smoothing kernel. The peak region of significance resulting from analysis of FA (see Figure 7 in the main manuscript) was used as a seed for deterministic fiber tractography with Camino software (28), enabling an investigation of the connectivity of this region with the rest of the brain. Tractography results demonstrated that this specific region of the medial/midline thalamus is structurally connected to medial-temporal lobe and PFC regions (Figure S4).

Statistical Analysis

The effects of CRH on neuroimaging measures was assessed using voxelwise paired-sample *t*-tests (CRH group_(post-pre) – Control group_(post-pre)) using fMRISat (<http://www.math.mcgill.ca/keith/fmrifat/>). To account for potential confounds, all regressions entered the variable age as a covariate. Whole-brain statistical analyses

were performed on FDG-PET, resting fMRI, and DTI measures, and thresholded using a $p < .01$, two-tailed uncorrected statistical threshold. Follow-up across-group analyses of the FDG-PET data in relation to AT were thresholded at $p < .05$, two-tailed uncorrected.

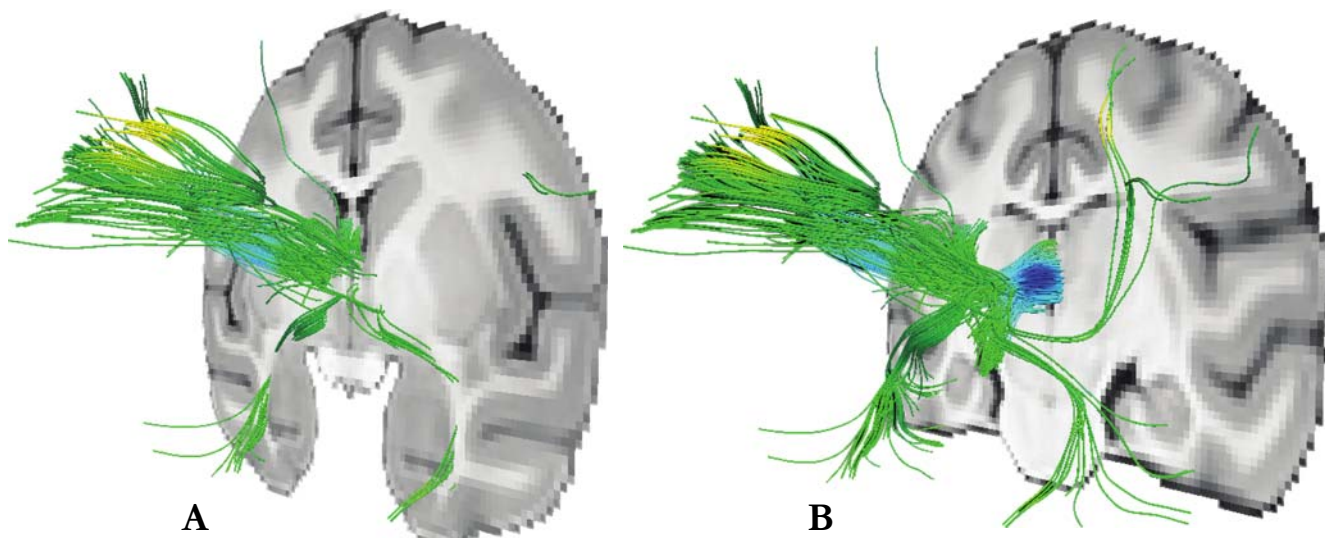


Figure S4. (A & B) Deterministic tractography, seeded in the thalamic region of significant FA change, is visualized on coronal MRIs that are rotated to view fiber connectivity projected along the A-P plane. This demonstrates that the seed region is connected to the prefrontal cortex and medial temporal lobe.

CRH Immunocytochemistry Performed in Fudge Laboratory

Approximately 1 year after AAV2 infusions, animals were euthanized by transcardiac perfusion with 0.9% heparinized-saline followed by 4% PFA in PBS, pH 7.4. The brains were extracted and fixed overnight in 4% PFA, and were then put through an increasing gradient of sucrose (10%, 20% and 30%) followed by sectioning at 40 μm on a freezing microtome. All sections were stored in cryoprotectant solution (30% ethylene glycol and 30% sucrose in 0.1 M phosphate buffer, pH 7.2) at -20°C . CRH expression was assessed by CRH immunoreactivity with the same commercial CRH antibody (Peninsula Labs, made in rabbit; 1:6000) used for the *in vitro* validation of the CRH viral vector construct described above (and see below for further details). Signal was visualized with biotinylated anti-rabbit secondary antibody and avidin-biotin reaction

(Vector Laboratories). 1:12 sections through the brain were immunostained for CRH. Sections were mounted on subbed slides, dehydrated in an increasing gradient of alcohols, cleared in xylene for 45 minutes, and coverslipped with Permount (Sigma, St Louis, MO).

The antibody used for the postmortem detection of CRH overexpression (anti-CRH, Peninsula Labs; T-4037), was previously characterized in rodents (31). To ensure that the Peninsula brand antibody had the same pattern as the well-established Olschowka antibody (anti-CRH, gift of Dr. John Olschowka) (32), we directly compared the two. Both antibodies are made in rabbit, the commercial antibody used synthetic peptide as the immunogen, and the Olschowka antibody is made against the ovine peptide (33). Neither antibody (Peninsula or Olschowka) had been used in the monkey, and we wanted to ensure that we had reliable staining. After determining the best dilutions, we then examined the distribution of labeled cells and fibers in the Ce, BST, and PVN resulting from each antibody. The labeling pattern was equivalent. We also compared labeling in *Macaca mulatta* and *Macaca fascicularis*, and found the distribution of labeled cells and fibers in these structures to be similar between the species. Finally, we examined the distribution of labeled cells in sections immunoreacted with antibody to sections labeled for CRH mRNA using in situ hybridization (R. Kovner 2014, unpublished observations), and found a similar distribution of cells through the rostrocaudal extent of the Ce as was observed with immunocytochemistry.

Measuring CRH Levels in Cerebrospinal Fluid

A radioimmunoassay established in our laboratory with an antibody (rC68 – 5/31/83 bleed) generously provided by Dr. Wylie Vale (Salk Institute for Biological Studies, La Jolla, CA) was used as previously described (34). All samples were run in triplicate in a single assay.

Table S1. Significant peaks in the FDG_PET analysis

Clusters demonstrating significant [CRH (post-pre) – Control (post-pre)] interaction				Local maxima for distinct brain regions within clusters			Location relative to anterior commissure		
Direction of effect	Hemisphere	Cluster	Cluster volume (mm ³)	Regions within cluster	Maximum t-value	p-value	x	y	z
Positive	Right	posterior hippocampus / visual cortex / pulvinar	296.63	posterior hippocampus	55.78	6.34E-06	15.000	-15.625	-4.375
				V1	19.89	1.39E-04	13.750	-23.125	1.875
				WM dorsal to hippocampus	15.99	2.66E-04	16.875	-10.625	-3.750
				anterior pulvinar bordering on the WM	12.04	6.17E-04	10.625	-11.875	5.625
	Crosses midline	prefrontal cortex	261.47	orbitofrontal cortex (Area 13M)	64.07	4.19E-06	-13.750	13.750	0.625
				ventromedial prefrontal cortex (Area14M)	46.70	1.08E-05	0.625	18.750	-1.250
				posterior orbitofrontal cortex (Area 47O) / OPro	35.18	2.53E-05	-17.500	10.000	-3.125
				orbitofrontal cortex (Area 14O)	21.83	1.05E-04	-3.125	15.625	-1.250
				frontopolar cortex (Area10)	19.72	1.42E-04	1.250	29.375	1.875
				ventrolateral prefrontal cortex (Area47)	16.70	2.34E-04	-15.625	19.375	5.000
	Left	dorsal amygdala / globus pallidus	100.34	dorsal amygdala (Ce region) / putamen	109.53	8.39E-07	-12.500	-1.250	-6.875
				external globus pallidus	46.08	1.13E-05	-7.500	-0.625	-1.250
	Right	orbitofrontal cortex	62.01	Area 13M	52.80	7.48E-06	12.500	13.750	0.000
	Left	cerebellum	40.28	cerebellum	40.08	1.71E-05	0.000	-19.375	-11.875
	Left	anterior temporal lobe	27.83	temporopolar cortex	26.66	5.79E-05	-13.125	6.250	-13.125
	Right	mid-cingulate cortex	22.22	cingulate sulcus (Area23C)	15.54	2.89E-04	6.875	-6.250	13.750
	Left	visual cortex	20.75	ventral V4	110.18	8.24E-07	-10.000	-18.125	-6.875
ventral V3				13.03	4.88E-04	-6.250	-19.375	-4.375	
Left	ventral temporal cortex	19.53	temporal area TL (36R)	18.95	1.60E-04	-16.250	-9.375	-15.000	
Right	superior temporal gyrus	11.23	superior temporal sulcus area 1 (ST1)	24.62	7.35E-05	26.250	1.250	-6.875	
			temporopolar proisocortex (TPPro)	7.01	2.98E-03	23.125	4.375	-11.250	
Negative	Left	posterior parietal lobe	73.00	dorsal V4	-53.39	7.24E-06	-18.750	-25.625	14.375
				parietal area PG	-36.76	2.21E-05	-20.625	-24.375	13.125
				dorsal parietal cortex	-16.03	2.64E-04	-11.250	-28.750	18.750
				V2	-7.65	2.32E-03	-8.125	-35.625	16.875
				temporoparietal area	-6.00	4.64E-03	-23.750	-20.625	10.000
	Left	somatosensory cortex	16.11	S2 / Area3b	-37.89	2.02E-05	-25.000	-3.125	4.375
	Left	posterior frontal lobe	14.89	Area 8A	-14.33	3.68E-04	-18.750	3.125	13.750
	Right	frontal lobe	8.30	Area 8A / principal sulcus	-12.20	5.92E-04	18.750	8.750	14.375

WM, white matter; OPro, orbital proisocortex

Table S2. Significant peaks in the Δ AT - Δ PET correlation

Clusters demonstrating significant [AT (post-pre) vs. PET (post-pre)] correlation				Local maxima for distinct brain regions within clusters			Location relative to anterior commissure			
Direction of effect	Hemisphere	Cluster	Cluster volume (mm ³)	Regions within cluster	Maximum t-value	p-value	x	y	z	
Positive	Right	posterior hippocampus / inferior pulvinar / parasubiculum	58.35	inferior pulvinar / parasubiculum	6.85	3.19E-03	10.625	-14.375	-3.125	
				WM dorsal to hippocampus	5.30	6.54E-03	17.500	-13.125	-4.375	
		orbitofrontal cortex	50.05	OPro	6.38	3.90E-03	-16.875	8.125	-3.125	
				Area 13M	6.12	4.39E-03	-10.000	15.000	1.250	
				temporopolar proisocortex	5.77	5.18E-03	-19.375	8.125	-4.375	
				gustatory cortex	4.07	1.34E-02	-21.250	8.125	-1.250	
		Right	orbitofrontal cortex	21.97	Area 13	6.04	4.55E-03	13.125	16.875	2.500
		Left	posterior hippocampus	16.36	posterior hippocampus	7.01	2.98E-03	-16.250	-12.500	-8.125
		Left	cerebellum / pons	15.14	cerebellum / pons	5.41	6.18E-03	-0.625	-20.000	-13.750
		Left	temporal cortex	11.23	temporal area TR, rostral part	6.11	4.41E-03	-16.875	-8.125	-15.000
		Left	globus pallidus	10.50	internal globus pallidus	6.69	3.41E-03	-7.500	-2.500	0.625
		Left	dorsal amygdala	10.01	BLD, IPAC, AA	6.90	3.12E-03	-13.125	3.125	-5.625
		Right	caudate / claustrum / ventral pulvinar	9.28	claustrum	6.75	3.32E-03	11.875	-9.375	6.250
		Left	ventromedial prefrontal cortex	9.03	Area 14O	6.24	4.15E-03	-1.250	18.125	-0.625
Negative	Left	visual cortex	10.25	V4D	-6.75	3.33E-03	-9.375	-32.500	18.125	
	Left			V2	-5.30	6.57E-03	-7.500	-35.625	16.875	

OPro, orbital proisocortex; BLD, basal nucleus of the amygdala, dorsal part; IPAC, interstitial nucleus of the posterior limb of the anterior commissure, AA, anterior amygdala area V4D, visual area V4, dorsal part

Table S3. Significant peaks in the functional connectivity analysis

Clusters demonstrating significant [CRH (post-pre) – Control (post-pre)] interaction				Local maxima for distinct brain regions within clusters			Location relative to anterior commissure		
Direction of effect	Hemisphere	Cluster	Cluster volume (mm ³)	Regions within cluster	Maximum t-value	p-value	x	y	z
Positive	Right	posterior orbitofrontal cortex	53.96	OPro / AI	129.44	5.08E-07	12.500	7.500	-4.375
	Right	dorsal amygdala	49.56	anterior amygdalar nucleus / medial nucleus	22.35	9.80E-05	8.125	1.250	-6.875
	Left	cerebellum	39.31	cerebellum	9.77	1.14E-03	-5.000	-30.000	-9.375
	Left	globus pallidus / thalamus	37.35	ventral anterior thalamic nucleus	53.90	7.03E-06	-5.000	-5.000	1.875
	Left	posterior orbitofrontal cortex	34.91	OPro / AI	18.85	1.63E-04	-11.875	8.125	-6.875
	Right	prefrontal cortex	10.01	WM ventral to Area8B	8.95	1.47E-03	7.500	13.750	15.625
Negative	Left	temporal cortex	184.81	superior temporal sulcus	-73.45	2.78E-06	-17.500	-0.625	-10.000
				Area TE	-23.23	8.74E-05	-18.125	1.250	-16.250
				temporopolar proisocortex (TPPro)	-20.26	1.31E-04	-21.250	5.000	-11.250
	Right	visual cortex	105.47	V1	-78.90	2.24E-06	18.750	-33.750	5.625
	Right	anterior temporal lobe	95.70	WM lateral to ventral putamen	-56.24	6.19E-06	16.875	-2.500	-7.500
				Area TE	-31.51	3.51E-05	21.250	-5.625	-16.875
				LGN / WM dorsal to hippocampus	-24.06	7.87E-05	13.750	-7.500	-6.250
				superior temporal sulcus	-6.58	3.57E-03	21.875	-5.625	-11.875
	Right	temporoparietal WM	85.45	deep WM of superior temporal gyrus	-51.24	8.19E-06	16.875	-15.000	2.500
				WM ventral to intraparietal sulcus	-18.78	1.65E-04	10.625	-15.000	10.000
	Right	visual cortex	79.10	V1	-96.53	1.23E-06	13.125	-41.875	7.500
	Left	posterior ventral temporal lobe / cerebellum	59.57	cerebellum	-34.91	2.58E-05	-11.875	-18.125	-8.750
				posterior hippocampus	-32.09	3.32E-05	-15.625	-17.500	-4.375
	Left	brain stem	19.29	cerebral peduncle	-14.19	3.79E-04	-5.000	-16.250	-10.000
	Left	mid-hippocampus / ventral putamen	16.85	WM dorsal to hippocampus	-41.15	1.58E-05	-15.000	-7.500	-5.625
Left	parietal cortex	16.60	opercular part of parietal Area PG	-21.56	1.09E-04	-20.625	-20.000	13.125	
Right	striatum	8.79	lateral putamen	-30.80	3.76E-05	17.500	-1.250	3.125	

AI, anterior insular cortex; WM, white matter; OPro, orbital proisocortex; LGN lateral geniculate nucleus

Table S4. Significant peaks in the DTI analysis (MD)

Clusters demonstrating significant [CRH (post-pre) – Control (post-pre)] interaction				Local maxima for distinct brain regions within clusters			Location relative to anterior commissure		
Direction of effect	Hemisphere	Cluster	Cluster volume (mm ³)	Regions within cluster	Maximum t-value	p-value	x	y	z
Positive	Left	visual cortex	61.52	V1	38.74	1.89E-05	-4.375	-39.375	6.875
				V2	11.98	6.25E-04	-8.125	-33.750	6.250
	Right	caudate / septum / stria terminalis / fornix	55.18	lateral septum / caudate	20.34	1.30E-04	2.500	1.875	5.000
	Left	cerebellum	33.20	cerebellum	62.99	4.41E-06	-5.625	-17.500	-11.250
	Right	visual cortex	32.47	dorsal V4 / TEO	23.81	8.12E-05	28.750	-23.125	-0.625
	Left	parietal cortex	17.58	PGOp	26.33	6.01E-05	-25.000	-16.875	13.750
	Right	precuneus	16.36	PGM	19.18	1.55E-04	1.250	-30.000	16.875
	crosses the midline	cerebellum	16.11	cerebellum	10.90	8.26E-04	2.500	-25.625	-10.625
	Left	visual cortex	10.74	V2	15.40	2.97E-04	-18.750	-33.125	9.375
	Right	ventral temporal cortex	9.77	superior temporal gyrus	23.11	8.87E-05	27.500	-5.000	-10.625
Negative	Right	frontal cortex	296.14	Area 8A, dorsal part	-109.75	8.34E-07	15.000	9.375	19.375
	Right			Area 9 / Area 46, dorsal part	-6.16	4.31E-03	16.250	15.625	13.750
	Right	visual cortex	10.25	V1	-43.81	1.31E-05	3.750	-46.875	-3.125

TEO, temporal area TE, occipital part; PGOp, parietal area PG, opercular part; PGM parietal area PG, medial part

Table S5. Significant peaks in the DTI analysis (RD)

Clusters demonstrating significant [CRH (post-pre) – Control (post-pre)] interaction				Local maxima for distinct brain regions within clusters			Location relative to anterior commissure		
Direction of effect	Hemisphere	Cluster	Cluster volume (mm ³)	Regions within cluster	Maximum t-value	p-value	x	y	z
Positive	Right	caudate / septum / stria terminalis / fornix	231.93	lateral septum / caudate	51.77	7.94E-06	2.500	1.250	5.000
				WM dorsal to putamen	25.29	6.78E-05	13.125	-5.000	9.375
				caudate / internal capsule	19.46	1.48E-04	10.000	-3.125	7.500
	Left	visual cortex	55.18	V1	24.35	7.59E-05	-4.375	-38.750	7.500
				V2	8.28	1.85E-03	-8.125	-32.500	5.625
	Right	dorsal thalamus	52.25	ventral lateral thalamic nucleus	12.26	5.85E-04	8.125	-6.875	6.875
	Left	cerebellum	29.05	cerebellum	18.33	1.77E-04	-5.625	-17.500	-8.750
	crosses midline	cerebellum	26.86	cerebellum	15.41	2.97E-04	5.000	-25.625	-11.875
	Left	motor cortex	26.12	Area 4	17.84	1.92E-04	-17.500	-1.250	15.000
				Area 6	10.22	9.99E-04	-16.875	1.875	14.375
	Left	visual cortex	18.80	V2	22.85	9.18E-05	-18.750	-33.125	9.375
	Right	prefrontal cortex	15.87	Area 47	36.75	2.22E-05	18.750	23.750	6.875
	Right	precuneus	14.65	PGM	18.89	1.62E-04	0.625	-30.625	17.500
	Right	cerebellum	13.43	cerebellum	30.69	3.80E-05	5.000	-30.000	-20.000
	Right	motor cortex	13.18	Area 6	9.92	1.09E-03	16.875	1.875	20.625
	Right	temporal cortex	8.30	superior temporal gyrus	26.17	6.12E-05	27.500	-5.000	-11.250
	Negative	Right	frontal cortex	260.50	Area 8	-80.34	2.13E-06	13.125	15.625
Right		visual cortex	9.77	V1	-43.70	1.32E-05	3.750	-46.875	-3.125

WM, white matter; PGM parietal area PG, medial part

Table S6. Significant peaks in the DTI analysis (AD)

Clusters demonstrating significant [CRH (post-pre) – Control (post-pre)] interaction				Local maxima for distinct brain regions within clusters			Location relative to anterior commissure		
Direction of effect	Hemisphere	Cluster	Cluster volume (mm ³)	Regions within cluster	Maximum t-value	p-value	x	y	z
Positive	Right	temporal cortex	84.96 TPO		105.05	9.51E-07	25.000	-17.500	8.125
	Right	temporal cortex	49.07 TEO		35.80	2.40E-05	29.375	-25.000	-3.750
	Left	cerebellum / pons	32.23 cerebellum / pons		14.18	3.80E-04	-3.750	-17.500	-8.750
	Left	parietal cortex	27.34 PGOp		24.53	7.43E-05	-23.750	-14.375	13.125
	Left	temporal cortex	24.41 entorhinal cortex		15.65	2.83E-04	-8.750	-2.500	-18.125
				TLR(36R)	12.16	5.98E-04	-12.500	-1.250	-20.625
	Left	visual cortex	23.93 V1		38.24	1.97E-05	-8.125	-35.000	7.500
	Left	visual cortex	18.31 V1		14.44	3.60E-04	-5.625	-40.000	5.625
	Right	precuneus	18.31 PEC		21.81	1.06E-04	0.625	-30.000	16.875
	Left	visual cortex	17.82 V2		28.70	4.64E-05	-21.875	-28.750	-3.750
	Right	temporal cortex	16.85 TE		16.54	2.40E-04	24.375	-5.625	-14.375
	Right	motor cortex	15.87 Area 6		9.82	1.12E-03	17.500	1.250	20.625
	Right	caudate / septum / stria terminalis / fornix	12.45 lateral septum / caudate		8.55	1.68E-03	1.875	2.500	5.625
	Right	somatosensory cortex	8.79 Area 2		20.61	1.25E-04	26.875	-4.375	8.125
	Left	motor cortex	8.30 Area 6		25.84	6.36E-05	-10.625	-0.625	18.125
Negative	Right	frontal cortex	359.62 Area 8		-137.56	4.24E-07	14.375	8.750	18.750
			Area 6		-56.20	6.20E-06	8.125	9.375	18.750
	Left	cerebellum	28.81 cerebellum		-31.42	3.54E-05	-14.375	-29.375	-17.500
	Right	visual cortex	24.90 V1		-19.54	1.46E-04	16.875	-38.125	-3.125
	Left	temporal cortex	11.96 superior temporal gyrus		-35.88	2.38E-05	-26.875	0.000	-8.750
	Right	visual cortex	10.25 V1		-37.15	2.14E-05	4.375	-46.875	-3.125

TPO, temporal parieto-occipital association area; TEO, temporal area TE, occipital part; PGOp, parietal area PG, opercular part; TLR(36R), temporal area TL, rostral part; PEC, parietal area PE, caudal part TE, temporal area TE;

Table S7. Significant peaks in the DTI analysis (FA)

Clusters demonstrating significant [CRH (post-pre) – Control (post-pre)] interaction				Local maxima for distinct brain regions within clusters			Location relative to anterior commissure		
Direction of effect	Hemisphere	Cluster	Cluster volume (mm ³)	Regions within cluster	Maximum t-value	p-value	x	y	z
Positive	Right	visual cortex	18.31	V1	61.74	4.68E-06	10.625	-38.125	15.000
	Right	visual cortex	17.58	collateral sulcus / ventral V3	28.16	4.91E-05	15.625	-33.125	-3.750
	Right	primary motor cortex	17.33	Area 4	8.30	1.84E-03	15.625	-4.375	18.125
	Right	visual cortex	10.50	V1 / V2	28.32	4.83E-05	15.625	-22.500	0.000
Negative	Right	visual cortex	48.34	V3A	-30.76	3.77E-05	12.500	-33.125	10.000
	Left	visual cortex	41.50	V2	-28.05	4.97E-05	-15.000	-34.375	13.125
	Left	intraparietal sulcus	32.23	V3A	-19.57	1.46E-04	-12.500	-26.875	6.875
	crosses midline	midline thalamus	16.11	mediodorsal thalamic nucleus	-10.73	8.66E-04	-1.875	-6.250	2.500
				mediodorsal thalamic nucleus	-6.03	4.58E-03	4.375	-6.875	1.875
	Right	corpus callosum	12.70	splenium	-17.10	2.18E-04	3.750	-16.250	5.000
	Right	visual cortex	8.30	V1	-10.39	9.51E-04	10.625	-43.750	-5.625
	Left	visual cortex	8.06	V1 / V2	-16.95	2.24E-04	-24.375	-34.375	4.375

Supplemental References

1. Paxinos G, Huang X, Petrides M, Toga A (2009): *The rhesus monkey brain in stereotaxic coordinates*. 2nd ed. San Diego: Academic Press.
2. Lim MM, Hammock EA, Young LJ (2004): A method for acetylcholinesterase staining of brain sections previously processed for receptor autoradiography. *Biotechnic and Histochemistry*. 79:11-16.
3. Fox AS, Shelton SE, Oakes TR, Davidson RJ, Kalin NH (2008): Trait-like brain activity during adolescence predicts anxious temperament in primates. *PLoS ONE*. 3:e2570.
4. Shackman AJ, Fox AS, Oler JA, Shelton SE, Davidson RJ, Kalin NH (2013): Neural mechanisms underlying heterogeneity in the presentation of anxious temperament. *Proceedings of the National Academy of Sciences of the United States of America*. 110:6145-6150.
5. Oler JA, Fox AS, Shelton SE, Rogers J, Dyer TD, Davidson RJ, et al. (2010): Amygdalar and hippocampal substrates of anxious temperament differ in their heritability. *Nature*. 466:864-868.
6. Fox AS, Kalin NH (2014): A Translational Neuroscience Approach to Understanding the Development of Social Anxiety Disorder and Its Pathophysiology. *The American journal of psychiatry*.
7. Emborg ME, Joers V, Fisher R, Brunner K, Carter V, Ross C, et al. (2010): Intraoperative intracerebral MRI-guided navigation for accurate targeting in nonhuman primates. *Cell transplantation*. 19:1587-1597.
8. Emborg ME, Hurley SA, Joers V, Tromp do PM, Swanson CR, Ohshima-Hosoyama S, et al. (2014): Titer and product affect the distribution of gene expression after intraputaminaal convection-enhanced delivery. *Stereotact Funct Neurosurg*. 92:182-194.
9. Truwit CL, Liu H (2001): Prospective stereotaxy: a novel method of trajectory alignment using real-time image guidance. *Journal of magnetic resonance imaging : JMRI*. 13:452-457.
10. Brodsky EK, Block WF, Alexander AL, Emborg ME, Ross CD, Sillay KA (2011): Intraoperative device targeting using real-time MRI. *Biomedical Sciences and Engineering Conference (BSEC), 2011*, pp 1-4.
11. Grabow B, Block W, Alexander AL, Hurley S, CD R, Sillay K, et al. (2012): Extensible real-time MRI platform for intraoperative targeting and monitoring.

ISMRM Nineteenth Annual Scientific Meeting and Exhibition, poster presentation #1585. Melbourne, Australia.

12. Grabow BP, Oler JA, Riedel M, Fekete EM, Kovner R, brodsky EK, et al. (2014): Alteration of Molecular Neurochemistry: MRI-guided Delivery of Viral Vectors to the Primate Amygdala. *ISMRM Twenty-First Annual Scientific Meeting and Exhibition, oral presentation #672. Milan, Italy.*
13. Brady ML, Raghavan R, Block W, Grabow B, Ross C, Kubota K, et al. (2015): The Relation between Catheter Occlusion and Backflow during Intraparenchymal Cerebral Infusions. *Stereotact Funct Neurosurg.* 93:102-109.
14. Santos JM, Wright GA, Pauly JM (2004): Flexible Real-Time Magnetic Resonance Imaging Framework. 1048-1051.
15. Radau PE, Pintilie S, Flor R, Biswas L, Oduneye SO, Ramanan V, et al. (2012): VURTIGO : Visualization Platform for Real-Time , MRI-Guided Cardiac Electroanatomic Mapping. 244-253.
16. Birn RM, Shackman AJ, Oler JA, Williams LE, McFarlin DR, Rogers GM, et al. (2014): Evolutionarily conserved prefrontal-amygdalar dysfunction in early-life anxiety. *Mol Psychiatry.* 19:915-922.
17. Fox AS, Oakes TR, Shelton SE, Converse AK, Davidson RJ, Kalin NH (2005): Calling for help is independently modulated by brain systems underlying goal-directed behavior and threat perception. *Proc Natl Acad Sci U S A.* 102:4176-4179.
18. Fox AS, Oler JA, Shackman AJ, Shelton SE, Raveendran M, McKay DR, et al. (2015): Intergenerational neural mediators of early-life anxious temperament. *Proc Natl Acad Sci U S A.* 112:9118-9122.
19. Kalin NH, Shelton SE, Fox AS, Oakes TR, Davidson RJ (2005): Brain regions associated with the expression and contextual regulation of anxiety in primates. *Biol Psychiatry.* 58:796-804.
20. Oler JA, Birn RM, Patriat R, Fox AS, Shelton SE, Burghy CA, et al. (2012): Evidence for coordinated functional activity within the extended amygdala of non-human and human primates. *Neuroimage.* 61:1059-1066.
21. Oler JA, Fox AS, Shelton SE, Christian BT, Murali D, Oakes TR, et al. (2009): Serotonin transporter availability in the amygdala and bed nucleus of the stria terminalis predicts anxious temperament and brain glucose metabolic activity. *J Neurosci.* 29:9961-9966.

22. Avants BB, Tustison NJ, Song G, Cook PA, Klein A, Gee JC (2011): A reproducible evaluation of ANTs similarity metric performance in brain image registration. *Neuroimage*. 54:2033-2044.
23. Avants BB, Yushkevich P, Pluta J, Minkoff D, Korczykowski M, Detre J, et al. (2010): The optimal template effect in hippocampus studies of diseased populations. *Neuroimage*. 49:2457-2466.
24. Vincent JL, Patel GH, Fox MD, Snyder AZ, Baker JT, Van Essen DC, et al. (2007): Intrinsic functional architecture in the anaesthetized monkey brain. *Nature*. 447:83-86.
25. Cox RW (1996): AFNI: software for analysis and visualization of functional magnetic resonance neuroimages. *Comput Biomed Res*. 29:162-173.
26. Jo HJ, Saad ZS, Simmons WK, Milbury LA, Cox RW (2010): Mapping sources of correlation in resting state fMRI, with artifact detection and removal. *Neuroimage*. 52:571-582.
27. Woolrich MW, Jbabdi S, Patenaude B, Chappell M, Makni S, Behrens T, et al. (2009): Bayesian analysis of neuroimaging data in FSL. *Neuroimage*. 45:S173-186.
28. Cook PA, Bai Y, Nedjati-Gilani S, Saunarine KK, Hall MG, Parker GJ, et al. (May, 2006): Camino: Open-Source Diffusion-MRI Reconstruction and Processing. *14th Scientific Meeting of the International Society for Magnetic Resonance in Medicine*. Seattle, WA, USA, pp 2759.
29. Chang LC, Jones DK, Pierpaoli C (2005): RESTORE: robust estimation of tensors by outlier rejection. *Magnetic resonance in medicine : official journal of the Society of Magnetic Resonance in Medicine / Society of Magnetic Resonance in Medicine*. 53:1088-1095.
30. Zhang H, Yushkevich PA, Alexander DC, Gee JC (2006): Deformable registration of diffusion tensor MR images with explicit orientation optimization. *Medical image analysis*. 10:764-785.
31. Tagliaferro P, Morales M (2008): Synapses between corticotropin-releasing factor-containing axon terminals and dopaminergic neurons in the ventral tegmental area are predominantly glutamatergic. *J Comp Neurol*. 506:616-626.
32. Olschowka JA, O'Donohue TL, Mueller GP, Jacobowitz DM (1982): The distribution of corticotropin releasing factor-like immunoreactive neurons in rat brain. *Peptides*. 3:995-1015.

33. Vale W, Spiess J, Rivier C, Rivier J (1981): Characterization of a 41-residue ovine hypothalamic peptide that stimulates secretion of corticotropin and beta-endorphin. *Science*. 213:1394-1397.
34. Raper J, Stephens SB, Henry A, Villarreal T, Bachevalier J, Wallen K, et al. (2014): Neonatal amygdala lesions lead to increased activity of brain CRF systems and hypothalamic-pituitary-adrenal axis of juvenile rhesus monkeys. *J Neurosci*. 34:11452-11460.